UNIVERSITÀ DEGLI STUDI DI PADOVA

DIPARTIMENTO DI BIOLOGIA

Corso di Laurea magistrale in Environmental Sustainability and Education

TESI DI LAUREA

Biostratigraphic study and aleoecological response of calcareous nannoplankton assemblages during the Middle Eocene Climatic Optimum (MECO) at ODP Site 702 (South Atlantic Ocean)

Relatore: Prof.ssa /CLAUDIA AGNINI
Dipartimento di Geosciences

Laureando: SEYED MEHRGAN HOSSEININEJAD HASSANKIADEH
2090074

ANNO ACCADEMICO 2024/2025

Abstract

This Master's thesis presents a biostratigraphic study and paleoecological reconstruction of calcareous nannoplankton assemblages across the Middle Eocene Climatic Optimum (MECO) at ODP Site 702, located in the central area of the Islas Orcadas Rise (50°56.760′S, 26°22.122′W, 3,083.4 m water depth) in the South Atlantic Ocean. The MECO represents a transient yet significant global warming event that occurred approximately 40 million years ago and is associated with major perturbations in ocean temperature, carbonate chemistry, and biological communities. Calcareous nannoplankton, due to their high evolutionary rates, widespread distribution, and well-preserved fossil record, offer valuable tools for tracking biotic responses to such environmental changes and for refining stratigraphic frameworks.

The primary goal of this thesis is to develop a robust age model for the sedimentary succession encompassing the MECO at Site 702. High-resolution qualitative and quantitative analyses were conducted on calcareous nannofossil assemblages prepared through smear slide methodology. A total of 48 samples were analyzed from Hole 702B, covering a stratigraphic interval of approximately 26.8 meters. Nannofossil assemblages were examined under polarized light microscopy to evaluate taxonomic composition, preservation state, and fluctuations in abundance. Semi-quantitative and relative abundance counts were performed to estimate the distribution of selected taxa per mm² and the percentage abundance of taxa. The biostratigraphic zonation applied follows the schemes of Martini (1971), Okada & Bukry (1980), and Agnini et al. (2014), allowing integration with previously established bioevents and enabling temporal calibration based on magneto- and cyclostratigraphic age models.

The examined interval falls within Zone NP16 (Martini, 1971), Subzone CP14a (Okada & Bukry, 1980), and Zone CNE14 (Agnini et al., 2014).

Compared to deeper sites in the South Atlantic or equatorial regions (e.g., Sites 1260 and 929), the intermediate paleodepth of Site 702 (~2200–2300 m) appears to have allowed for better preservation of calcareous nannofossils across the MECO interval. This relatively favorable preservation has facilitated the recognition of discrete bioevents and paleoecological signals, including subtle changes in assemblage composition and relative abundance. The succession at

Site 702 confirms the broad-scale reliability of MECO-associated bioevents previously identified at other locations, supporting their applicability as global stratigraphic markers.

In summary, the integration of biostratigraphic, paleoecological, and chronostratigraphic data at Site 702 provides a detailed account of calcareous nannoplankton dynamics during a critical episode of global climatic change. The findings contribute to our understanding of biotic responses to extreme warmth in Earth's history and enhance the resolution of stratigraphic correlation across different ocean basins during the Middle Eocene.

Table of Contents

Summary

This thesis presents a high-resolution biostratigraphic and paleoecological investigation of calcareous nannofossil assemblages from sediments recovered at ODP Site 702, located on the Islas Orcadas Rise in the South Atlantic Ocean. The studied interval spans the Middle Eocene Climatic Optimum (MECO), a transient global warming event dated to approximately 40 Ma. Calcareous nannofossils, which are calcitic remains of unicellular phytoplankton (primarily Haptophytes), were selected as the main biostratigraphic tool due to their high evolutionary rates, wide geographic distribution, and excellent preservation potential in marine sediments.

The micropaleontological analysis focused on the identification and quantification of nannofossil taxa across a stratigraphic interval of approximately 0.89 million years. Samples were prepared using the smear slide technique and observed under cross-polarized light microscopy. The preservation of nannofossils in the studied section was generally good, allowing for reliable recognition of key biostratigraphic markers. The association was dominated by *Reticulofenestra*, *Coccolithus*, *Chiasmolithus*, and *Sphenolithus*, with variations in abundance and diversity closely linked to paleoenvironmental changes during the MECO.

Biostratigraphic events (biohorizons) were defined based on the First and Last Occurrences of marker species and were correlated with standard biozonation schemes, including Martini (1971), Okada & Bukry (1980), and more recent Mediterranean schemes such as Fornaciari et al. (2010) and Agnini et al. (2014). The succession studied corresponds to Zone NP16 (Martini), Subzone CP14a (Okada & Bukry), Subzones MNP16A–MNP16Ba (Fornaciari), and Zone CNE14 (Agnini).

The age model adopted for this study follows the cyclostratigraphic tuning of Westerhold & Röhl (2013), as applied to Site 702 by Rivero-Cuesta et al. (2019). The model integrates $\delta^{13}C$ and $\delta^{18}O$ isotope curves with Fe content fluctuations derived from XRF data to calibrate the studied interval

to orbital forcing. The stratigraphy spans from ~40.62 to ~39.73 Ma, crossing Chron C19n, the full extent of Chron C18r, and the base of Chron C18n.2n.

The results provide a robust biostratigraphic and biochronological framework for the MECO interval in the South Atlantic, enabling correlation with other Atlantic and Tethyan sites. The documented assemblage variations and bioevents reflect significant paleoceanographic shifts linked to climatic warming, ocean stratification, and changes in fertility. This work contributes to the broader understanding of marine biotic responses to Paleogene climatic perturbations and confirms the suitability of Site 702 as a reference section for high-resolution stratigraphic and paleoecological studies.

1. PALEOCLIMATE CONTEXT

1.1. Paleoclimatic evolution during the Paleogene

The Paleogene period, spanning from approximately 66 to 23 million years ago, represents a crucial phase in Earth's climatic history. It marks the transition from the Mesozoic's warm greenhouse climate to the cooler, more variable conditions of the Neogene. This interval is bounded by the Cretaceous-Paleogene (K-Pg) boundary at ~66 Ma and the Oligocene-Miocene boundary at ~23.03 Ma, according to the GTS2020 timescale (Gradstein et al., 2020) . The Paleogene documents major climatic perturbations, significant reorganizations in ocean-atmosphere circulation, and evolutionary changes in marine plankton groups, particularly calcareous nannoplankton (Agnini et al., 2014; Bown et al., 2004).

A key method for reconstructing paleoclimatic changes involves the analysis of stable isotope records, especially the composite $\delta^{18}O$ and $\delta^{13}C$ curves derived from benthic foraminifera. The most recent and comprehensive compilation is presented by Westerhold et al. (2020), who integrated high-resolution data from over 50 deep-sea drilling sites into an astronomically tuned age model spanning the last 66 million years. This refined isotopic framework offers a continuous archive of global deep-sea temperature and carbon cycle evolution throughout the Cenozoic.

Oxygen isotopic ratios ($\delta^{18}O$) are expressed in per mil (‰) and indicate the deviation in the ratio of heavy to light oxygen isotopes ($^{18}O/^{16}O$) in a sample relative to an international standard (Ruddiman, 2007). The formula is:

$$\delta^{18}O = \left(\frac{(^{18}O \,/\, ^{16}O)sample}{(^{18}O \,/\, ^{16}O)standard} - 1 \right) \times 1000$$

Where:

- **$\delta^{18}O$** = the delta notation for oxygen isotopic composition, expressed in parts per thousand (‰).

- **$(^{18}O/^{16}O)_{sample}$** = the ratio of heavy to light oxygen isotopes measured in the sample (e.g., carbonate from benthic foraminifera).

- **$(^{18}O/^{16}O)_{standard}$** = the same ratio in a standard reference material (commonly VPDB or VSMOW).

- **× 1000** = converts the result into per mil (‰), allowing fine-scale comparison of isotopic differences.

Common international standards include Vienna Standard Mean Ocean Water (VSMOW), Vienna Pee Dee Belemnite (VPDB), and Standard Light Antarctic Precipitation (SLAP) https://www.iaea.org/resources/safety-standards.

When measured in biogenic carbonates (e.g., foraminifera), $\delta^{18}O$ acts as a paleothermometer. The empirical relationship between $\delta^{18}O$ and seawater temperature was first described by Epstein et al. (1951) and later refined. The paleotemperature equation is:

$$T\,(^{\circ}\mathrm{C}) = 16.5 - 4.3(\delta^{18}O_{\text{sample}} - \delta^{18}O_{\text{seawater}}) + 0.14(\delta^{18}O_{\text{sample}} - \delta^{18}O_{\text{seawater}})^2$$

Where:

- T is the paleotemperature
- $\delta^{18}O$_sample is the measured isotopic composition of the carbonate
- $\delta^{18}O$_seawater is the assumed isotopic composition of seawater

This equation demonstrates that lower $\delta^{18}O$ values correspond to higher temperatures. However, during periods of large ice sheet expansion, ^{16}O is preferentially stored in ice, enriching the ocean in ^{18}O. Thus, both temperature and ice volume changes influence $\delta^{18}O$ signals (Ruddiman, 2007).

Throughout the Paleocene and much of the Eocene, Earth experienced greenhouse conditions with little or no permanent ice sheets. Under these conditions, $\delta^{18}O$ variations mainly reflect deep-sea temperature changes. The early Paleogene $\delta^{18}O$ trend, as illustrated in Westerhold et al. (2020), shows a gradual long-term cooling interrupted by transient warming events, including the

Paleocene-Eocene Thermal Maximum (PETM) and the Middle Eocene Climatic Optimum (MECO)—the primary focus of this study.

Carbon isotopes ($\delta^{13}C$) provide additional insight into global biogeochemical cycles. $\delta^{13}C$ variations reflect changes in organic productivity, carbon burial, and the exchange of carbon among reservoirs. Positive $\delta^{13}C$ excursions often indicate enhanced organic carbon burial, while negative excursions reflect rapid oxidation or release of isotopically light carbon, such as during the PETM (Westerhold et al., 2020; Ruddiman, 2007).

In summary, the Paleogene represents a key interval for understanding how Earth's climate and biosphere responded to both gradual trends and abrupt perturbations. The integration of high-resolution isotopic records—particularly those from **O**DP Site 702, provides a valuable framework to evaluate these changes and their significance within the broader context of Earth's climate evolution.

Oxygen Isotopes

In recent decades, high-resolution records of $\delta^{18}O$ variations throughout the Cenozoic have been developed based on benthic foraminiferal data from numerous ocean drilling sites (Zachos et al., 2001; 2008; Miller et al., 2005; Westerold et al, 2020). These composite datasets capture both long-term climatic evolution and short-term perturbations on orbital timescales. Over the Paleogene, the $\delta^{18}O$ record reveals a long-term cooling trend that began in the Late Cretaceous and reached its peak warmth during the Early Eocene Climatic Optimum (EECO, ~50 Ma).

Following the Early Eocene Climatic Optimum (EECO), $\delta^{18}O$ values show a long-term increasing trend, reflecting a gradual cooling of deep ocean temperatures throughout the middle and late Eocene (Westerhold et al., 2020). Despite this trend, the Earth remained in a greenhouse state, with no evidence of major continental ice sheets. The so-called "doubthouse" interval bridges the peak warmth of the EECO and the transition into the icehouse world, but glacial conditions were not yet established. A major shift occurred near the Eocene–Oligocene boundary (~34 Ma), marking the rapid onset of sustained Antarctic glaciation and the beginning of a true icehouse regime.

Superimposed on this long-term trend are numerous briefs and abrupt negative $\delta^{18}O$ excursions, or hyperthermals, including well-known events like the Paleocene-Eocene Thermal Maximum (PETM) and the Middle Eocene Climatic Optimum (MECO). These events are interpreted as episodes of rapid global warming and often coincide with major disruptions to the global carbon cycle documented by Zachos et al. (2008), Sluijs et al. (2007), and Westerhold et al. (2020).

Many of these hyperthermals are believed to be paced by astronomical forcing, particularly eccentricity, obliquity, and precession cycles (Lourens et al., 2005). They are typically characterized by simultaneous negative excursions in $\delta^{18}O$ (indicating warming) and $\delta^{13}C$ (indicating a carbon cycle perturbation), collectively referred to as Carbon Isotope Excursions (CIEs). These geochemical fingerprints are crucial for recognizing and correlating transient climatic events across globally distributed marine sedimentary sequences.

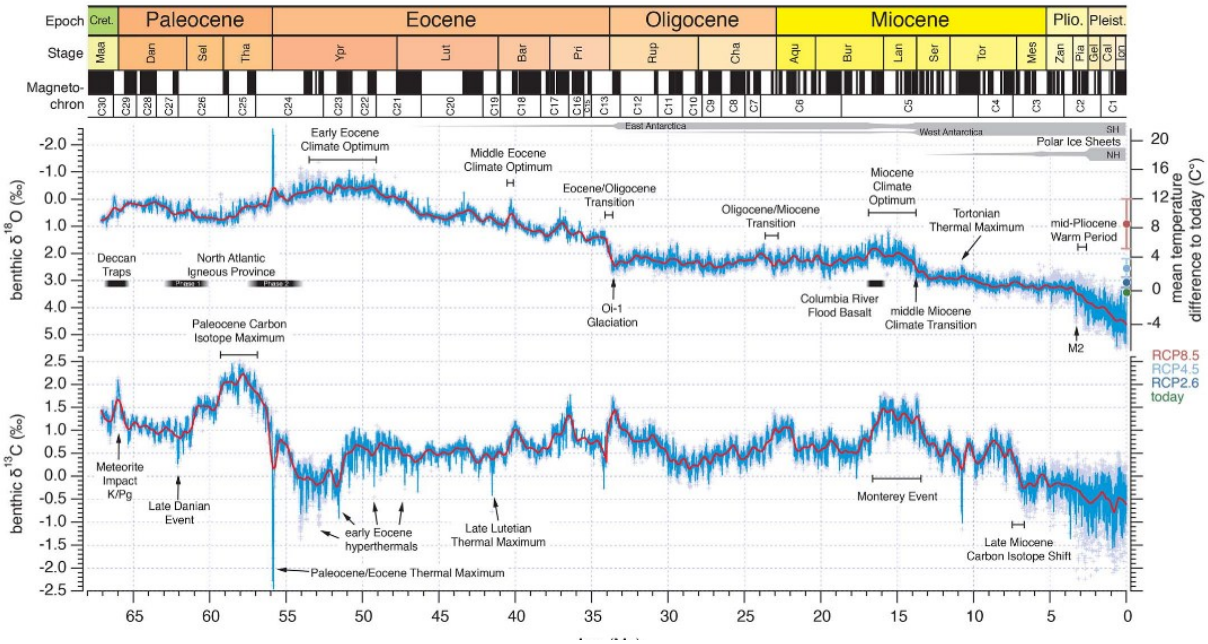

Figure 1.1. Global compilation of astronomically tuned benthic foraminiferal $\delta^{18}O$ and $\delta^{13}C$ records spanning the last 66 million years, modified from Westerhold et al. (2020). The $\delta^{18}O$ curve (top panel) reflects changes in deep-sea temperature and, from the Eocene–Oligocene boundary onward, also captures the development of polar ice sheets. The $\delta^{13}C$ curve (bottom panel) documents long-term carbon cycle evolution, including major perturbations such as the Paleocene–Eocene Thermal Maximum (PETM), Early Eocene hyperthermals, the Middle Eocene Climatic Optimum (MECO), and the Monterey Event. Colored climate states (hothouse, warmhouse, coolhouse, and icehouse) highlight key transitions, while the upper time scale shows epoch and stage boundaries alongside

magnetic polarity chrons. This compilation, known as the CENOGRID, represents the most up-to-date isotopic framework for interpreting Cenozoic climate evolution.

The Paleogene period is characterized by several climatic fluctuations, among which the so-called hyperthermal events stand out. These brief but intense warming episodes punctuate the long-term cooling trend that followed the peak warmth of the Early Eocene Climatic Optimum (EECO) (Zachos et al., 2008; Westerhold et al., 2020). One of the most prominent and well-studied of these episodes is the Paleocene–Eocene Thermal Maximum (PETM), which occurred at approximately 56 million years ago, near the Paleocene–Eocene boundary, as calibrated in the latest GTS2020 timescale (Gradstein et al., 2020).

The PETM serves as a key example for understanding the mechanisms that govern rapid climatic and geochemical disturbances in Earth's history. It is marked by a pronounced negative excursion in oxygen isotopes (δ18O), corresponding to a global temperature rise of about 5–8°C, and a simultaneous negative excursion in carbon isotopes (δ13C), typically around 3‰ (Kennet & Scott, 1991; Zachos et al., 2005). These signals suggest a massive release of isotopically light carbon—estimated to exceed 2000 GtC—into the ocean-atmosphere system (Zachos et al., 2005; Archer et al., 1997). The precise source remains debated, but hypotheses include the destabilization of methane hydrates or volcanic outgassing (Zachos et al., 2005; Storey et al., 2007). The carbon release would have triggered a decrease in ocean pH, leading to widespread acidification and dissolution of deep-sea carbonates, pushing the Carbonate Compensation Depth (CCD) to shallower depths (Zachos et al., 2005).

This disturbance in ocean chemistry is recorded in sedimentary sequences by the presence of clay-rich layers below the CCD and the decline or extinction of deep-sea benthic foraminifera. The PETM also saw a proliferation of calcareous plankton, anomalous dinoflagellate blooms, and the early dispersal of mammals (Sluijs et al., 2006; Storey et al., 2007; Lourens et al., 2005). It is followed by other less intense but notable events, such as ETM2 (~53.5 Ma) and ETM3 (~52.5 Ma), each associated with similar but more subdued isotopic and ecological perturbations (Westerhold et al., 2020).

Between 52 and 50 Ma, Earth experienced a sustained warm interval known as the Early Eocene Climatic Optimum (EECO). This phase stands out for its exceptionally high sea surface and deep-

sea temperatures, elevated pCO_2 levels, and the overall stability of greenhouse conditions (Westerhold et al., 2020). However, a gradual increase in δ18O values from ~50 to ~34 Ma indicates a long-term cooling trend, eventually leading to the establishment of permanent Antarctic glaciation at the Eocene-Oligocene boundary (Westerhold et al., 2020; Bohaty et al., 2009; Pagani et al., 2006).

This cooling phase represents a transition from the sustained warmth of the Early Eocene Climatic Optimum (EECO) toward the major reorganization of Earth's climate at the Eocene–Oligocene Transition (EOT). It is characterized by a stepwise increase in $\delta^{18}O$ values, reflecting episodic cooling events and evolving carbon cycle dynamics (Westerhold et al., 2020). The most notable among these is the Middle Eocene Climatic Optimum (MECO), a warming event that occurred around 40.0 to 40.6 Ma and spanned approximately 500 thousand years (Bohaty & Zachos, 2003; Bohaty et al., 2009).

The Middle Eocene Climatic Optimum (MECO), dated to approximately 40 Ma, is characterized by a gradual negative excursion in $\delta^{18}O$ values, reflecting a sustained global temperature rise over ~500 kyr (Bohaty & Zachos, 2003; Westerhold et al., 2020). Unlike shorter hyperthermal events such as the PETM or ETM2, the MECO exhibits a more complex and muted $\delta^{13}C$ signal (Bohaty et al., 2009), suggesting a distinct carbon cycle perturbation that lacks the abrupt negative spike typically associated with massive carbon release. Recent interpretations propose that this atypical carbon isotope response may result from a combination of enhanced volcanic CO_2 outgassing and increased silicate weathering feedbacks, which buffered the $\delta^{13}C$ signal and prolonged the warming (Henehan et al., 2020). Rather than acting as a precursor to the Eocene–Oligocene Transition (EOT), the MECO is now regarded as a transient climatic anomaly embedded within the broader cooling trajectory of the middle to late Eocene (Westerhold et al., 2020).

While this thesis will not delve exhaustively into each component of isotope geochemistry, it is important to understand the mechanisms behind $\delta^{13}C$ variability. The carbon isotope record reflects shifts in the balance of carbon reservoirs, biological productivity, and organic carbon storage. Processes such as increased volcanic CO_2 emissions, the oxidation of organic carbon, or decreased silicate weathering can lead to positive or negative $\delta^{13}C$ excursions. Meanwhile, silicate weathering and organic carbon burial act as long-term negative feedbacks by drawing CO_2 from the atmosphere and promoting climate stabilization (Ruddiman, 2007; Henehan et al., 2020).

Understanding the MECO within this broader paleoclimatic and geochemical context provides essential insight into the resilience and sensitivity of the Earth's climate system during the Paleogene. The following sections will focus on the stratigraphic, isotopic, and paleoecological records at ODP Site 702 to investigate how this event was expressed in the South Atlantic region.

1.2. The Middle Eocene Climatic Optimum (MECO)

1.2.1. The Middle Eocene Climatic Optimum: The $\delta^{18}O$ and $\delta^{13}C$ record

The Middle Eocene Climatic Optimum (MECO) is a transient global warming event that occurred approximately between 40.5 and 40.0 million years ago, identified through significant changes in stable isotope records. First defined by Bohaty and Zachos (2003), the MECO has since been studied extensively through high-resolution stable isotope analyses conducted on sediment cores retrieved during multiple Ocean Drilling Program (ODP) expeditions, particularly at Sites 1051 and 1260 (Bohaty et al., 2009; Edgar et al., 2010; Henehan et al., 2020).

Key records contributing to the identification of the MECO include benthic foraminiferal isotopic data from ODP Leg 113 (Site 689) and Legs 119 and 120 (Sites 738 and 748) in the Southern Ocean. These records show parallel trends in $\delta^{18}O$ and $\delta^{13}C$, indicating both a substantial increase in temperature and a disturbance in the carbon cycle. Benthic foraminifera such as *Nuttallides* and *Cibicidoides*, alongside fine-fraction carbonate samples (<63 μm), were analyzed to construct these curves (Bohaty & Zachos, 2003). Subsequent studies at additional ODP sites—such as Site 1260 in the equatorial Atlantic and Site 748 in the Southern Ocean—have expanded our understanding of the MECO through higher-resolution records and multiproxy approaches (Bohaty et al., 2009; Edgar et al., 2010; Henehan et al., 2020) .

The MECO is characterized by a gradual lightening of $\delta^{18}O$ values, which reflects ocean warming. While this progression is slower than the rapid shifts seen in short-lived Paleogene hyperthermals such as the PETM and ETM2, it is notably more transient than the multi-million-year-long EECO. Although initially recognized in the Southern Ocean, further investigations have confirmed the MECO's global relevance, with isotopic and micropaleontological evidence from both

hemispheres and multiple ocean basins (Bohaty et al., 2009; Agnini et al., 2014; Henehan et al., 2020; van der Ploeg et al., 2022)

This warming phase spans approximately 500 kyr and is often associated with a concurrent negative shift in $\delta^{13}C$, interpreted as the result of a large-scale carbon cycle perturbation. The global signature of these isotope anomalies has helped refine the temporal framework of the MECO, placing its onset near 40.6 Ma and its termination around 40.0 Ma (Henehan et al., 2020; van der Ploeg et al., 2022).

To better understand the scope and timing of this climatic anomaly, researchers have examined variations in carbonate content and isotopic ratios across numerous DSDP and ODP sites spanning the 43 to 38 Ma interval. These multi-proxy datasets support the classification of the MECO as a key middle Eocene hyperthermal event—distinct for its intermediate duration and complex carbon cycle response—and a pivotal interval for studying long-term climate sensitivity and feedbacks in a high-CO_2 world (Bohaty et al., 2009; Rivero-Cuesta et al., 2019; Henehan et al., 2020; van der Ploeg et al., 2022).

1.2.2. The Age of MECO

The Middle Eocene Climatic Optimum (MECO) was first dated by Bohaty and Zachos (2003), who placed the peak of the warming phase at approximately 41.5 Ma. However, later studies have refined both the onset and duration of the event. Thanks to improved chronological tools, such as magnetostratigraphy, subsequent authors (e.g., Jovane et al., 2007; Sexton et al., 2006; Bohaty et al., 2009; Agnini et al., 2011) proposed a more constrained timeline, placing the onset of the $\delta^{18}O$ lightening at around 40.6 Ma and estimating the total duration of the MECO to be about 500 thousand years (kyr).

The MECO is now recognized to have begun around 40.5 Ma, with a duration of approximately 500 kyr, based on orbitally tuned, high-resolution isotope stratigraphy (Henehan et al., 2020; van der Ploeg et al., 2022). Earlier estimates, such as the 41.5 Ma age proposed by Bohaty and Zachos (2003), were based on preliminary age models that have since been revised significantly. The updated chronology eliminates previous inconsistencies between records from the Southern Ocean and Equatorial Atlantic, reinforcing a coherent temporal framework for the event. Crucially, the

strong agreement of $\delta^{18}O$ and $\delta^{13}C$ anomalies across multiple, geographically distant sites highlights not only the global extent of the MECO but also its synchronicity. This alignment of isotopic signals from diverse ocean basins underscores the event's role as a globally coordinated perturbation in the Earth system (Henehan et al., 2020; van der Ploeg et al., 2022).

1.2.3. The characterization of the MECO

The Middle Eocene Climatic Optimum (MECO) was a transient global warming event that occurred around 40.5 million years ago, disrupting the long-term cooling trend that defined much of the middle and late Eocene. Unlike earlier, more abrupt events like the PETM, the MECO lasted approximately 400–500 kyr, leaving a prominent signal in deep-sea sediment records across the globe (Henehan et al., 2020; van der Ploeg et al., 2022).

Initial estimates by Bohaty & Zachos (2003) placed the MECO peak at ~41.5 Ma, but this was later shown to be inaccurate due to a flawed age model. Subsequent studies, using improved chronologies, refined the timing to ~40.5 Ma. later works such as Sexton et al. (2006), Jovane et al. (2007), and Agnini et al. (2011) provided more refined age control, supported by magneto- and biostratigraphic data. In particular, the well-studied Contessa Highway section (Italy) allowed for detailed calibration using isotopic signals and magnetochrons. Here, the the peak of the MECO is positioned between the top of Chron C18r and the base of Subchron C18n.2n, with its onset estimated at approximately 40 Ma and a total duration of about 600 kyr (Bohaty et al., 2009). These estimates are widely considered the most reliable, given the improved chronological framework and agreement with multiple sections. (Figure 1.4)

The MECO is primarily identified by a gradual negative shift in benthic and planktonic foraminiferal $\delta^{18}O$ values, reflecting a deep-sea temperature increase of approximately 3–6°C. This trend is seen from ~40.6 Ma, with minimum values (peak of the MECO) close to 40.0 Ma, followed by a rapid recovery in $\delta^{18}O$ by ~39.9 Ma. The amplitude of $\delta^{18}O$ negative excursion is ~1.0‰ in most records, though some sites (e.g., ODP 1051) record even greater values, up to 1.5‰. (Figure 1.3) (Bohaty et al., 2009; Agnini et al., 2011; Henehan et al., 2020; van der Ploeg et al., 2022).

The $\delta^{13}C$ signal during the MECO is more variable and generally exhibits a modest negative excursion when compared to other Paleogene hyperthermals. This contrasts with the pronounced and synchronous $\delta^{13}C$ and $\delta^{18}O$ excursions of the PETM, which reflect a rapid and massive

injection of isotopically light carbon into the ocean-atmosphere system (Sluijs et al., 2007; Zeebe et al., 2009). In the case of the MECO, however, the carbon isotope pattern appears to reflect spatially heterogeneous processes, such as regional shifts in marine productivity, remineralization rates, and ocean circulation, rather than a single, abrupt carbon source (Bohaty et al., 2009; Henehan et al., 2020; van der Ploeg et al., 2022). Despite this variability, the co-occurrence of $\delta^{13}C$ and $\delta^{18}O$ anomalies across multiple ocean basins supports the interpretation of the MECO as a globally significant disturbance of the ocean-atmosphere system.

ODP Site 702, located on the northeastern flank of the Islas Orcadas Rise in the South Atlantic, is particularly important for understanding the regional paleoceanographic response to the MECO. This site offers a well-preserved and stratigraphically complete sedimentary record across the middle Eocene, allowing for high-resolution analysis of calcareous nannofossil assemblages and stable isotopes (Rivero-Cuesta et al., 2019). The MECO interval is clearly expressed within magnetochron C18r and biostratigraphically corresponds to Zone NP16 (Martini, 1971). Changes in nannofossil assemblages—such as the reduced abundance of *Reticulofenestra umbilicus* and fluctuations in *Sphenolithus* spp.—are interpreted as evidence of ecological stress linked to sustained surface ocean warming. These assemblage shifts are consistent with those reported from other sites (Agnini et al., 2014; Rivero-Cuesta et al., 2019), reinforcing the global reach and biotic impact of the MECO.

This event is thought to reflect complex climate feedbacks under sustained high atmospheric CO_2 levels. Proposed forcing mechanisms include increased volcanic outgassing, reduced silicate weathering efficiency, and alterations in nutrient cycling and ocean circulation—all of which may have contributed to the prolonged carbon cycle imbalance observed during the MECO (Henehan et al., 2020; van der Ploeg et al., 2022; Sluijs et al., 2013). (Figure 1.5)

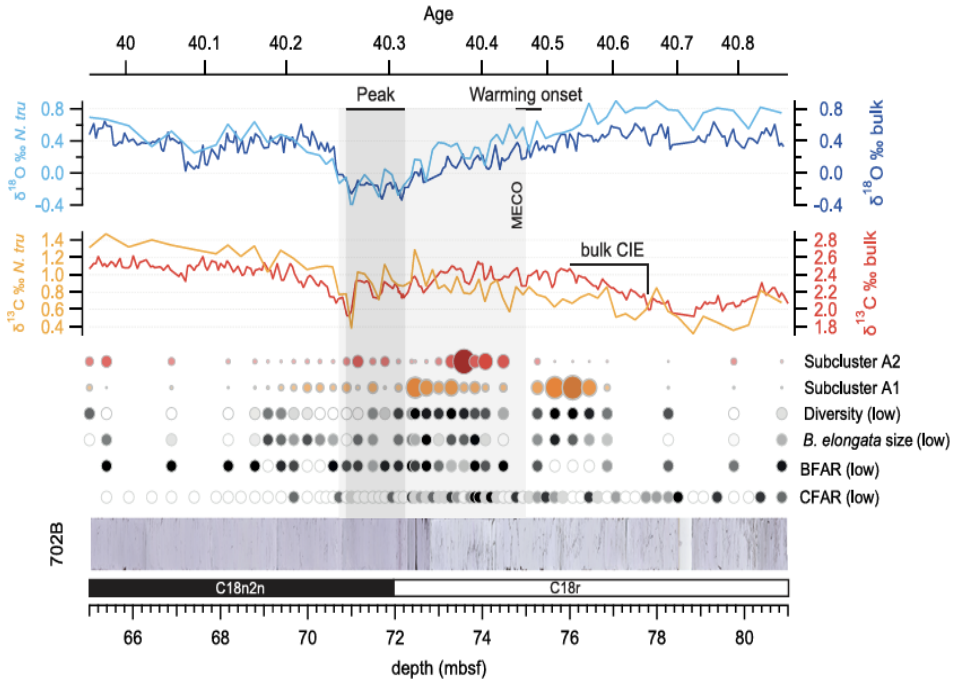

Figure 1.3. High-resolution $\delta^{18}O$ and $\delta^{13}C$ records from ODP Site 702 (South Atlantic), showing bulk and benthic foraminiferal isotope variations across the Middle Eocene Climatic Optimum (MECO). The data reveal a characteristic negative oxygen isotope excursion followed by a rapid recovery, and a more variable carbon isotope pattern with multiple negative peaks. These trends provide a refined view of the MECO at high southern latitudes and support the global expression of the event. Adapted from Rivero-Cuesta et al. (2019).

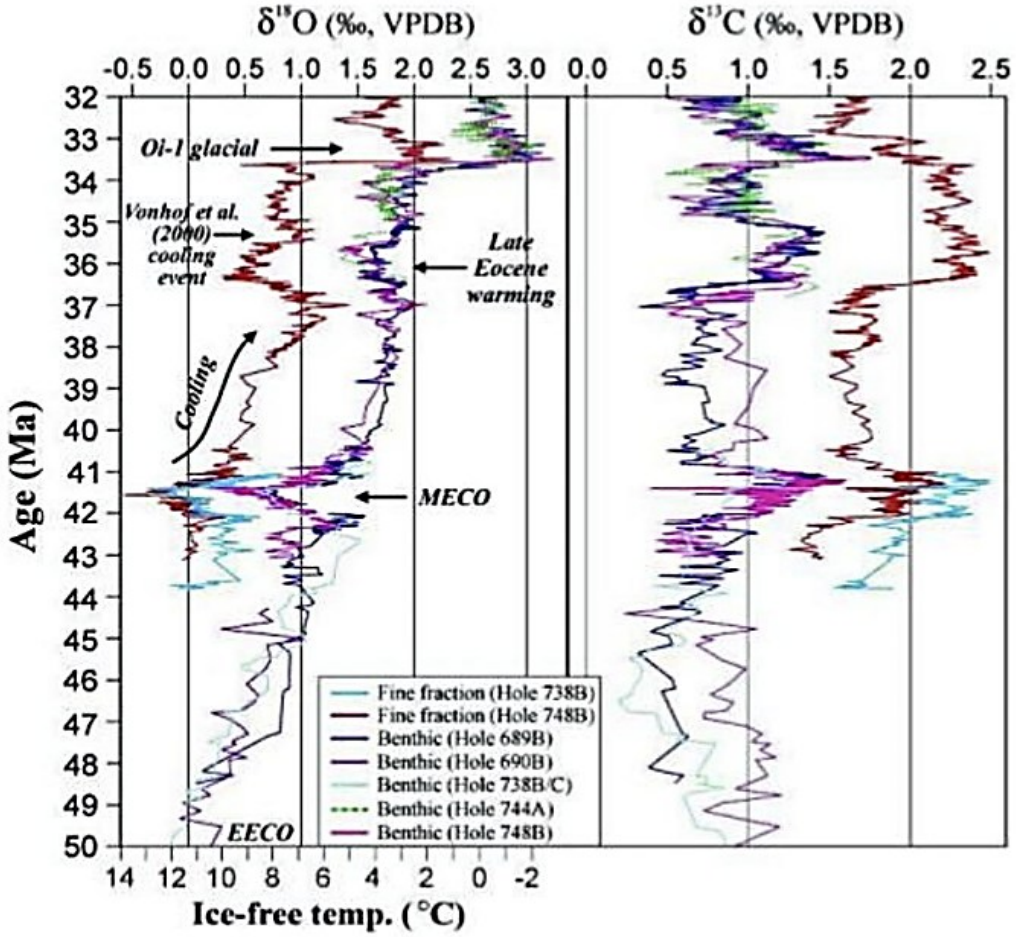

Figure 1.4. $\delta^{18}O$ and $\delta^{13}C$ records from Southern Ocean ODP sites, including fine-fraction and benthic foraminiferal data. The MECO is clearly identified as a perturbation in both isotope records centered around 41.5 Ma. This dataset was part of the original MECO identification but has since been updated by newer records. Adapted from Bohaty & Zachos (2003) and Bohaty et al. (2009).

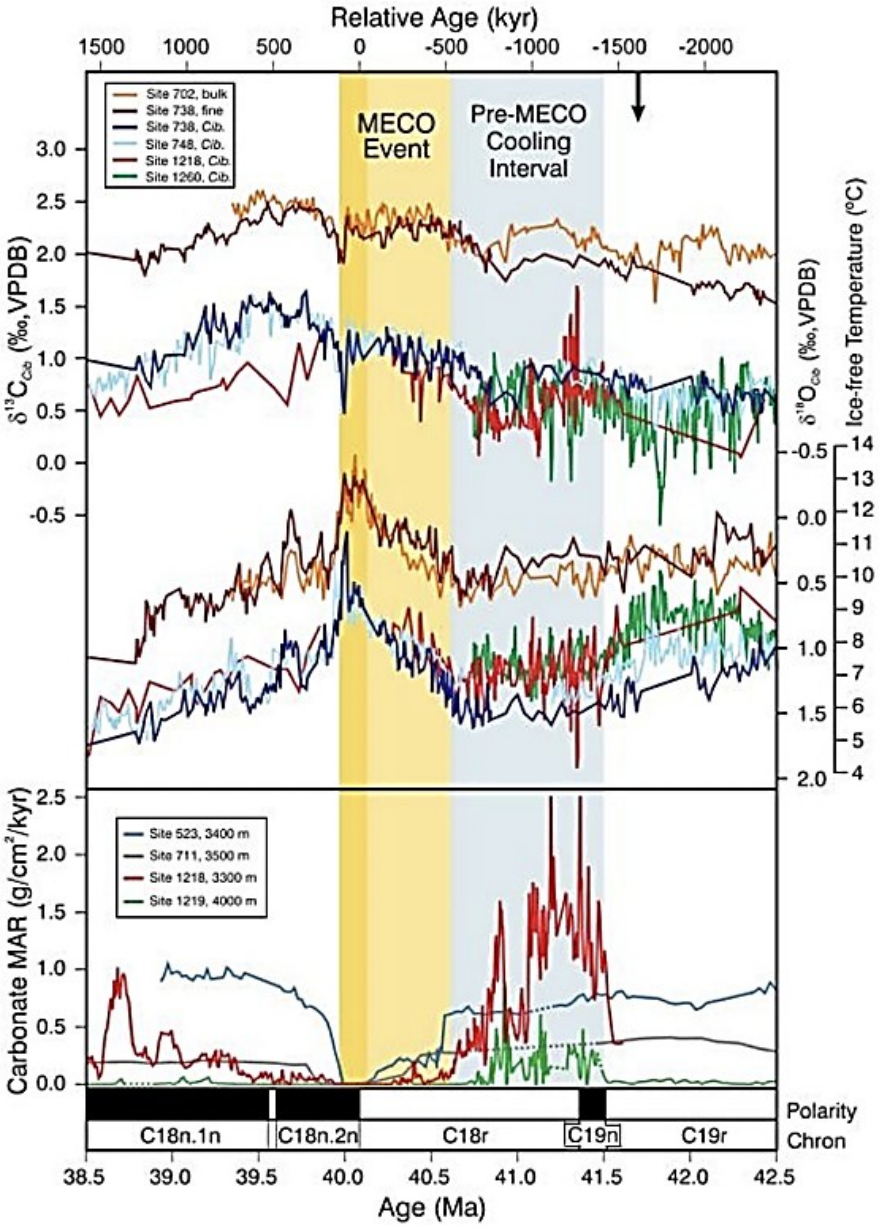

Figure 1.5. High-resolution $\delta^{18}O$ and $\delta^{13}C$ curves alongside carbonate accumulation data (MAR) from multiple sites during the MECO interval. The yellow band highlights the MECO event, while the blue marks the preceding cooling phase. The data illustrate the impact of the MECO on both isotopic trends and carbonate preservation. Adapted from Bohaty et al. (2009).

1.2.4. Relationship between changes in the carbon cycle, ocean acidification and temperature increase during the MECO

The Middle Eocene Climatic Optimum (MECO) represents a distinct and complex climatic perturbation that interrupted the long-term cooling trajectory of the middle Eocene. Spanning approximately 500–600 kyr, this event is notable not only for its duration but also for the significant modifications it induced in Earth's carbon cycle, ocean chemistry, and global temperatures. Despite extensive research, the precise trigger of the MECO remains debated, and no single mechanism has yet gained universal acceptance. Early hypotheses, such as volcanic outgassing, metamorphic decarbonation, or large-scale tectonic reorganization (Bohaty & Zachos, 2003; Bohaty et al., 2009), are now considered unlikely to account for the relatively short (~500–600 kyr) duration of the event. More recent studies have emphasized the role of internal Earth system feedbacks—such as a temporary weakening of the silicate weathering feedback, ocean circulation changes, or enhanced remineralization of organic matter—as potential amplifiers of MECO warming (van der Ploeg et al., 2018; Henehan et al., 2020). Furthermore, although astronomical forcing remains difficult to confirm conclusively due to the intermediate duration of the event, orbital pacing may have influenced the timing or sensitivity of climate feedbacks (Westerhold et al., 2014). Overall, the MECO likely represents a complex interaction between modest external forcing and nonlinear biogeochemical responses in a climate system already near a critical threshold (Zachos et al., 2012).

What distinguishes the MECO from earlier hyperthermal events of the Paleogene, such as the PETM and ETM2, is its occurrence during a long-term phase of global cooling. However, like those earlier events, MECO is associated with disruptions in the oceanic carbonate system. Marine sediment records from the Pacific Ocean show that both the Paleocene and Eocene were marked by alternations between intervals of deepening and shoaling of the calcite compensation depth (CCD) (Peterson & Backman, 1990; Lyle et al., 2005; Paelike et al, 2012). These fluctuations are thought to reflect dynamic responses in the global carbon cycle. During phases of CCD deepening, the accumulation of pelagic carbonates increases, forming what have been termed "Carbonate Accumulation Events" (CAEs) (Rea & Lyle, 2005). MECO is positioned shortly after CAE-3, around 41.6–40.8 Ma (Pälike et al., 2012).

A decline in carbonate mass accumulation rates (MARs) is observed at approximately 40.8 Ma, marking the onset of pronounced shoaling of the calcite compensation depth (CCD). Between 40.3

and 40.0 Ma, deep-sea sediments—especially in pelagic settings—record extremely low or near-zero MARs. This pattern is particularly pronounced in open-ocean environments because they are most sensitive to changes in carbonate chemistry and offer minimal buffering compared to marginal settings. Such shoaling is estimated to have raised the CCD by 500–1500 m, reaching paleodepths of approximately 2.5 km in several Pacific sites (Pälike et al., 2012). Supporting evidence for this pattern has been reported from the North Atlantic (Vahlenkamp et al., 2018), where high-resolution isotopic and carbonate records demonstrate synchronous carbonate dissolution and CCD shoaling. Similarly, data from the equatorial Atlantic (Menini, 2015) reinforce this interpretation, confirming a widespread, basin-scale response in carbonate preservation linked to peak MECO warming (Figure 1.6).

Importantly, the observed decline in carbonate mass accumulation rates (MARs) during the MECO is not solely attributed to reduced carbonate production in surface waters. Instead, multiple studies have emphasized the role of enhanced carbonate dissolution in response to ocean acidification, driven by the gradual release of isotopically light CO_2 into the ocean-atmosphere system. This process would have lowered seawater pH, increased carbonate solubility, and undermined carbonate preservation in pelagic sediments (Bohaty et al., 2009; Pälike et al., 2012). However, in more marginal or slope settings, terrigenous dilution—the increased input of non-carbonate (e.g., clay-rich) material—also played a critical role in reducing carbonate content, by physically diluting the biogenic carbonate fraction of sediments (Menini, 2015; Vahlenkamp et al., 2018). Thus, both chemical dissolution and terrigenous input must be considered when interpreting reduced MARs across different depositional environments during the MECO (Figure 1.7).

Among the plausible drivers of this acidification is a sustained increase in CO_2 degassing, possibly linked to volcanic arc activity, mantle plume upwelling, or metamorphic decarbonation during the early stages of Himalayan orogenesis (Kerrick & Caldeira, 1993, 1999; Cambray & Cadet, 1996; Bailey, 1993). These processes, although typically operating on longer timescales, may have contributed to a gradual buildup of atmospheric CO_2. Sustained high pCO_2 levels over several hundred thousand years would have required reinforcing feedbacks to maintain the climatic disturbance—such as suppressed silicate weathering or decreased organic carbon burial (Archer et al., 1997; Dickens, 2000).

The stable isotope record ($\delta^{18}O$ and $\delta^{13}C$) can be used to interpret past conditions and help understand the mechanisms and processes behind these events. A gradual decline in $\delta^{18}O$ values reflects deep-sea warming, while a coeval $\delta^{13}C$ negative excursion (~0.7‰), though spatially variable, is interpreted to represent a disruption in the oceanic carbon cycle, possibly due to reduced organic carbon burial or enhanced remineralization of respired carbon in the deep ocean (Henehan et al., 2020). One hypothesis suggests that this $\delta^{13}C$ signal may indicate destabilization of methane clathrates once a temperature threshold was crossed (Bohaty et al., 2009). However, similar isotopic responses could also result from enhanced remineralization of labile organic matter, changes in ocean stratification, or altered nutrient cycling (Pälike et al., 2012; Henehan et al., 2020).

An alternative hypothesis, proposed by Pälike et al. (2012), emphasizes the role of organic matter fluxes and nutrient cycling. They argued that variations in the ratio of labile to refractory organic carbon could have significantly altered the ocean's dissolved inorganic carbon (DIC) pool and pH. An increase in the availability of labile organic matter would have intensified respiration at depth, reducing carbonate saturation and promoting shoaling of both the CCD and lysocline.

Pälike et al. (2012) also propose that a decrease in the efficiency of continental weathering may have reduced CO_2 drawdown, reinforcing warming and acidification. Under normal conditions, rising temperatures enhance silicate weathering, which helps sequester atmospheric CO_2 and regulate climate. However, if this feedback were weakened or delayed, it could lead to prolonged greenhouse conditions. The return to pre-MECO conditions—marked by a relatively rapid deepening of the CCD over ~10 kyr—may be attributed to the reactivation of carbon sinks such as silicate weathering and burial of organic carbon (Corg).

In conclusion, the MECO illustrates a complex interplay between carbon cycle feedbacks, volcanic and tectonic activity, and ocean chemistry. Although uncertainties remain, sedimentary and isotopic records across multiple ocean basins—including Site 702—indicate that the MECO was a globally expressed event driven by prolonged disturbances in Earth’s carbon cycle.

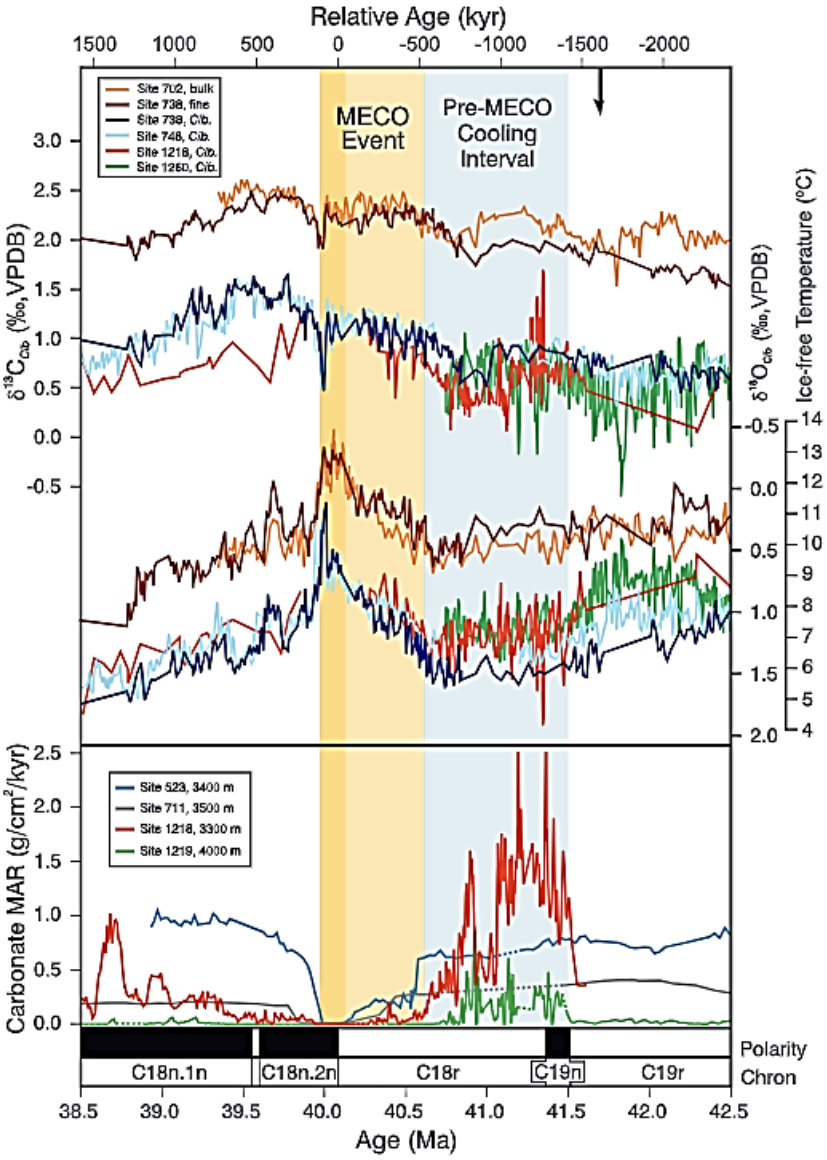

Figure 1.6 Benthic foraminiferal $\delta^{18}O$ and $\delta^{13}C$ profiles from multiple DSDP/ODP sites across the MECO interval, showing the gradual warming trend and carbon cycle disturbance between 40.6 and 40.0 Ma. The $\delta^{18}O$ negative shift (~1–1.5‰) indicates deep-sea warming and shoaling of the CCD. Modified from Bohaty et al. (2009).

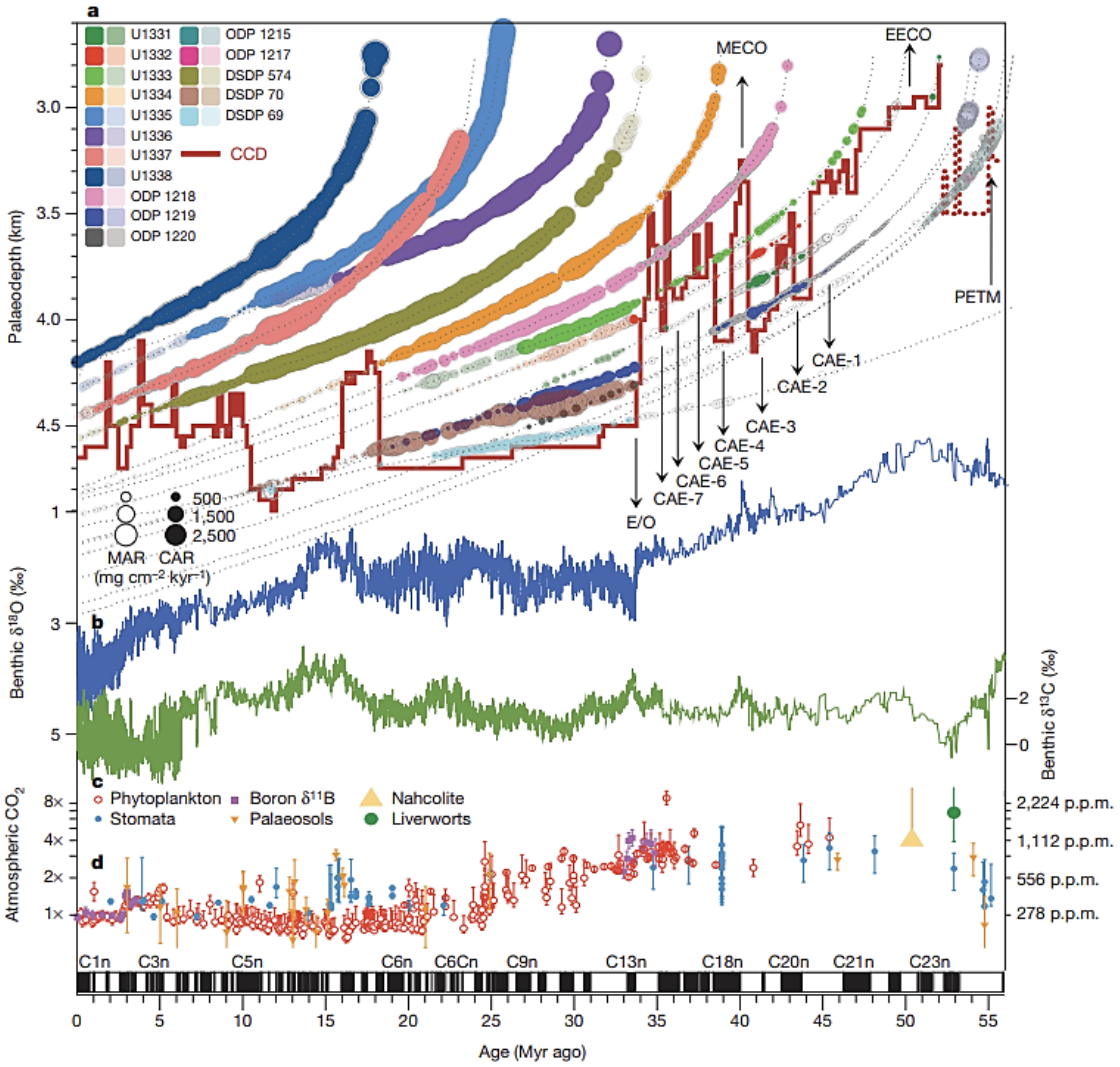

Figure 1.7. Carbonate accumulation patterns and estimated CCD depths in the equatorial Pacific across the early to middle Eocene, based on data from IODP Sites 1218 and 1219. The MECO is placed immediately after the CAE-3 event, during a pronounced reduction in carbonate MARs and a major shoaling of the CCD. The figure illustrates the anomalous nature of the MECO in disrupting the long-term deepening trend of the CCD and links the event to changes in carbon cycle dynamics, including reduced weathering efficiency and increased availability of labile organic carbon. Modified from Pälike et al. (2012).

2. THE OCEAN DRILLING PROGRAM, TECHNOLOGIES USED, LEG 114 (ODP SITE 702 – ISLAS ORCADAS RISE)

2.1. Historical Notes on Ocean Drilling Programs

The scientific investigation of Earth's history through deep-sea drilling has undergone remarkable advancement since its inception in the mid-20th century. Beginning with the Mohole Project in the late 1950s — an ambitious but ultimately incomplete effort to reach the Earth's mantle through oceanic crust — the concept of scientific ocean drilling evolved into a long-term international enterprise. These programs have profoundly influenced our understanding of global plate tectonics, oceanic crust formation, paleoclimate dynamics, and the long-term carbon cycle (Refs needed, for instance https://www.iodp.org/).

The Deep-Sea Drilling Project (DSDP), launched in 1968, marked the first systematic attempt to collect sediment cores from beneath the ocean floor. Operated by the Scripps Institution of Oceanography and supported by the U.S. National Science Foundation, DSDP used the drillship Glomar Challenger to recover continuous sequences of marine sediment. These cores provided one of the first direct evidence for seafloor spreading, magnetic striping, and the age progression of oceanic crust — pivotal observations that validated the theory of plate tectonics (Moore, 2009). In addition, DSDP allowed scientists to reconstruct paleoenvironmental and paleoclimatic conditions from the fossil and geochemical record preserved in ocean sediments (Kennett, 1982).

Building on the success of DSDP, the Ocean Drilling Program (ODP) was inaugurated in 1985 as a more advanced and globally coordinated scientific effort. Managed by Texas A&M University and supported by international partners through JOIDES (Joint Oceanographic Institutions for Deep Earth Sampling), ODP featured the drillship JOIDES Resolution — capable of drilling in deeper waters and retrieving longer, more complete sedimentary sequences. Over its 18-year lifespan, ODP completed more than 100 drilling legs at key geological sites across the globe. Its multidisciplinary approach integrated stratigraphy, geochemistry, micropaleontology, paleomagnetism, and sedimentology to produce high-resolution records of Earth's climate, oceanography, and lithospheric processes (IODP, 2024).

A major focus of ODP was to investigate the evolution of Earth's climate system, particularly during intervals of significant global change. One of its notable contributions was Leg 114, which targeted sites in the South Atlantic sector of the Southern Ocean, including ODP Site 702 on the

Islas Orcadas Rise. Drilling at Site 702 provided critical insights into Paleogene Ocean circulation, sediment dynamics, and climatic evolution, especially in relation to the opening of ocean gateways and the development of circum-Antarctic currents (Barker et al., 1988).

Following ODP, the program transitioned into the Integrated Ocean Drilling Program (IODP) in 2003, which expanded scientific goals to include not only Earth history but also the deep biosphere, subduction zone processes, and geohazards. The program also introduced multiplatform drilling, allowing operations in polar and shallow-water environments through the use of riser systems (Chikyū), mission-specific platforms, and icebreaker-supported expeditions. In 2013, IODP was restructured into its current framework — the International Ocean Discovery Program — with broader participation from Asia, Europe, North America, and beyond (JOIDES Resolution, 2024).

Collectively, these programs have recovered hundreds of kilometers of sediment and crustal core from over 1,500 sites worldwide. Their impact includes the development of a global stratigraphic framework based on biostratigraphy, magnetostratigraphy, and stable isotope stratigraphy. Moreover, they have clarified the timing, mechanisms, and feedbacks associated with major Earth system events such as the Paleocene–Eocene Thermal Maximum (PETM), the Middle Eocene Climatic Optimum (MECO), and the Eocene–Oligocene Transition (EOT) (Moore, 2009).

Today, the legacy of scientific ocean drilling remains central to geoscience. The samples, data, and methodologies developed by DSDP, ODP, and IODP continue to underpin research in paleoclimatology, paleoceanography, sedimentary geology, and planetary habitability. Sites such as ODP 702 remain invaluable archives for studying how Southern Hemisphere oceanography has influenced global environmental evolution.

Figure 2.1: Expedition 303, JOIDES Resolution in St. John's, Newfoundland (https://iodp.tamu.edu/index.html)

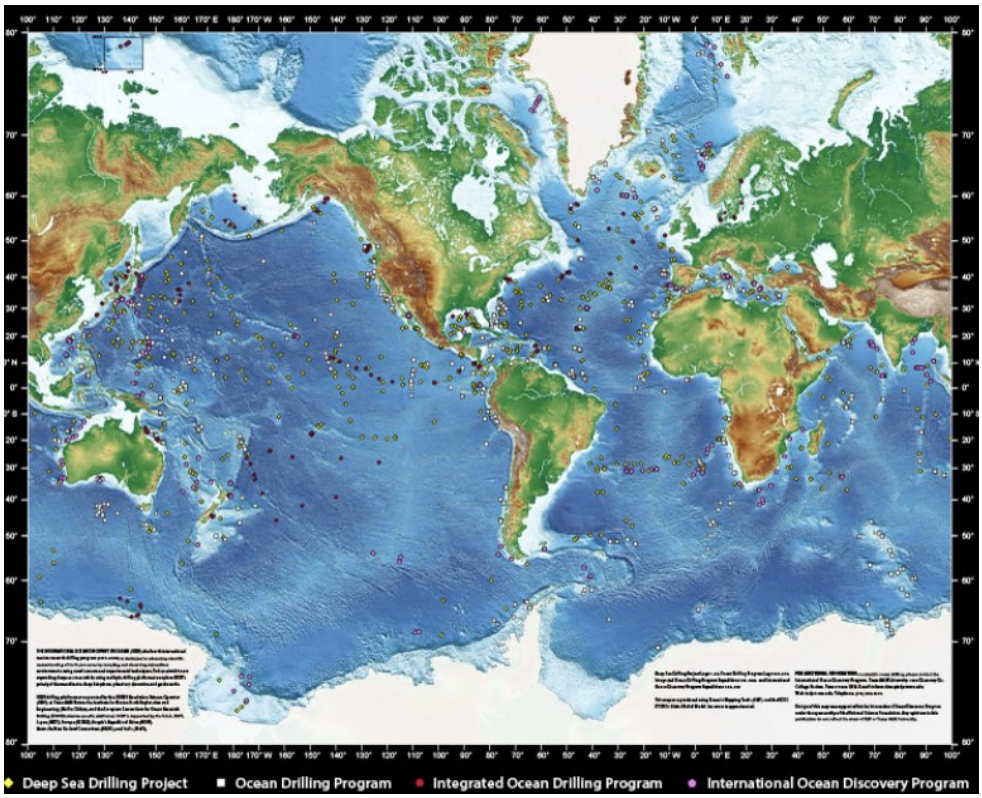

Figure 2.2: Global Map of Scientific Ocean Drilling Sites, this map illustrates the global distribution of drill sites from the Deep-Sea Drilling Project (DSDP), Ocean Drilling Program (ODP), and Integrated Ocean Drilling Program (IODP). It showcases the extensive reach of these programs across various ocean basins, highlighting the breadth of geological and paleoceanographic research conducted worldwide (Available at https://iodp.tamu.edu/scienceops/maps.html)

2.2. The JOIDES Resolution and the Technologies Used

The *JOIDES Resolution* is a deep-sea drilling vessel specifically designed for scientific exploration of the ocean floor. Commissioned in 1985, it has been the primary platform of the Ocean Drilling Program (ODP) and its successors, the Integrated Ocean Drilling Program (IODP) and International Ocean Discovery Program (IODP). Its name pays tribute to HMS *Resolution*, the ship used by Captain James Cook, symbolizing scientific exploration and global discovery (JOIDES Resolution, 2024).

The vessel measures 143 meters in length and is equipped with a tall derrick and dynamic positioning systems, which allow it to remain stable over a drill site even in deep water and rough sea conditions. The ship is capable of deploying more than 8,000 meters of drill pipe and can operate in water depths exceeding 7,000 meters. Its design allows for rotary drilling and coring in a wide range of sedimentary and oceanographic settings (IODP, 2024). Figure 2.2.2

The *JOIDES Resolution* employs a range of coring systems adapted to the mechanical properties of marine sediments:

- The **Advanced Piston Corer (APC)** is used for recovering soft, unconsolidated sediments. It provides high-quality, relatively undisturbed cores suitable for micropaleontological, geochemical, and sedimentological studies.
- The **Extended Core Barrel (XCB)** is used when sediments are firmer or slightly lithified. It combines rotary drilling with a softer coring head to improve recovery in transitional layers.
- The **Rotary Core Barrel (RCB)** is employed for drilling through consolidated or lithified sediments and basement rocks. Though core recovery is generally lower with RCB, it allows access to deeper and harder sequences.
- In later stages of the program, new experimental systems such as the **Pressure Coring System** and **Wireline Logging Tools** were developed and tested to retrieve samples under in situ pressure and obtain continuous geophysical logs (Kennett, 1982). (Figure 2.2.2)

One of the main strengths of the *JOIDES Resolution* lies in its ability to function as a floating laboratory. The vessel is equipped with a comprehensive suite of onboard laboratories, which are arranged around a central core handling area. These labs include:

- **Physical Properties Lab**, where cores are analyzed for bulk density, magnetic susceptibility, compressional wave velocity, and thermal conductivity.
- **Paleomagnetism Lab**, where the natural remanent magnetization (NRM) of the cores is measured to support magnetostratigraphic interpretations.
- **Geochemistry Lab**, where sediment and pore water samples are analyzed using techniques such as gas chromatography and inductively coupled plasma optical emission spectrometry (ICP-OES).
- **Micropaleontology and Paleontology Labs**, where calcareous nannofossils, foraminifera, diatoms, and radiolarians are identified and used to build biostratigraphic frameworks.
- **Sedimentology Lab**, where the lithological composition, grain size, sedimentary structures, and visual characteristics of the cores are described and documented (JOIDES Resolution, 2024). Figure 2.2.4

After cores are retrieved from the seafloor, they are split, labeled, photographed, and subjected to preliminary analysis following a standardized workflow. One half is archived, while the other is used for onboard measurements and sampling. All data generated during expeditions are logged in a central database and made accessible to the scientific community shortly after completion of the cruise (IODP, 2024).

In addition to core recovery, the *JOIDES Resolution* is equipped with **downhole logging tools** that can be deployed through the drill pipe to record geophysical parameters such as gamma ray activity, resistivity, and sonic velocity. These logs are used to correlate cores, identify lithological boundaries, and refine stratigraphic interpretations (https://iodp.tamu.edu/).

Since its launch, the *JOIDES Resolution* has supported hundreds of expeditions and contributed significantly to the development of marine geology, paleoclimatology, and stratigraphy. Its technical versatility and onboard facilities continue to make it one of the most valuable platforms for oceanographic research (Moore, 2009).

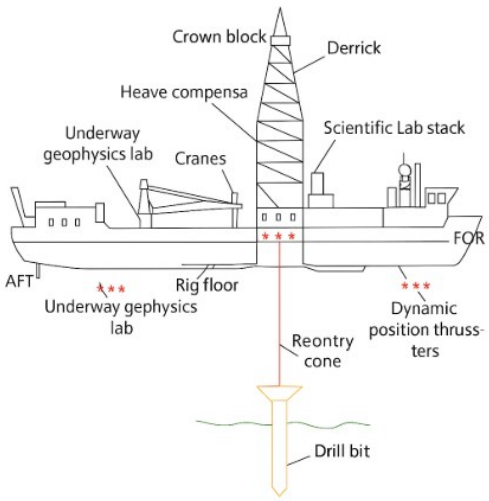

Figure 2.2.2 Structural schematic of the JOIDES Resolution and its drilling system. Labeled components include the derrick, drilling and positioning systems, onboard lab stack, and connection between the drill string and seafloor. This setup enables high-precision core recovery from oceanic sediments and crust.(JOIDES Resolution Science Operator)

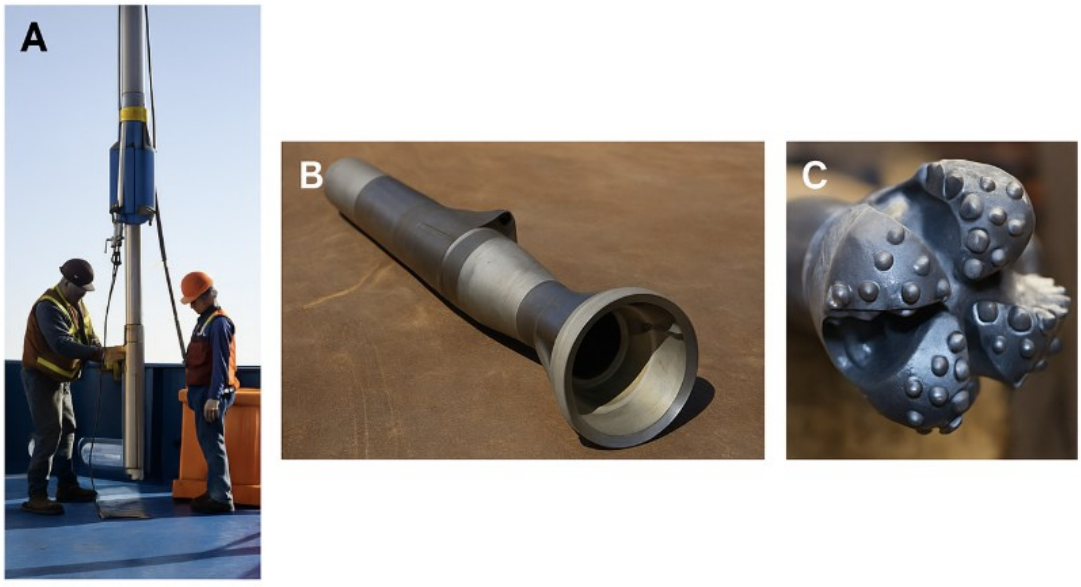

Figure 2.2.3: Coring systems employed on the JOIDES Resolution: A. Advanced Piston Corer (APC); B. Extended Core Barrel (XCB); C. Rotary Core Barrel (RCB). (https://joidesresolution.org)

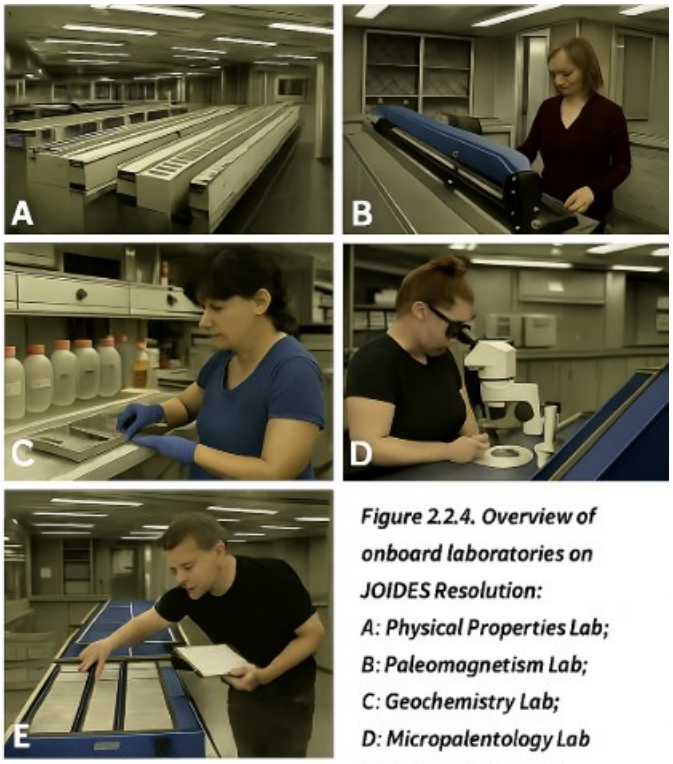

Figure 2.2.4. Overview of onboard laboratories on JOIDES Resolution:
A: Physical Properties Lab;
B: Paleomagnetism Lab;
C: Geochemistry Lab;
D: Micropalentology Lab
E: Sedimentology Lab

Source: Images from JOIES Resolution official website (https://joidesresoluti...

2.3. Leg 114: Islas Orcadas Rise, ODP Sites 701–704, Subantarctic South Atlantic

The Islas Orcadas Rise is an oceanic bathymetric high currently located in the subantarctic South Atlantic, northeast of the Falkland Plateau, between approximately 50° and 54°S latitude (Figure 2.3). It stretches over 500 km in a north-northwest to south-southeast direction and is up to 100 km wide. The present-day water depth across much of the crest ranges between 3000 and 3500 meters, while the flanks drop off sharply to depths exceeding 5000 meters in the adjacent Argentine and Vema Basins. The western margin, in particular, shows a steep bathymetric gradient as it transitions into the Argentine Basin, whereas the eastern side descends more gradually toward the Vema Channel (Fig. 2.3; Barker & Kennett, 1988).

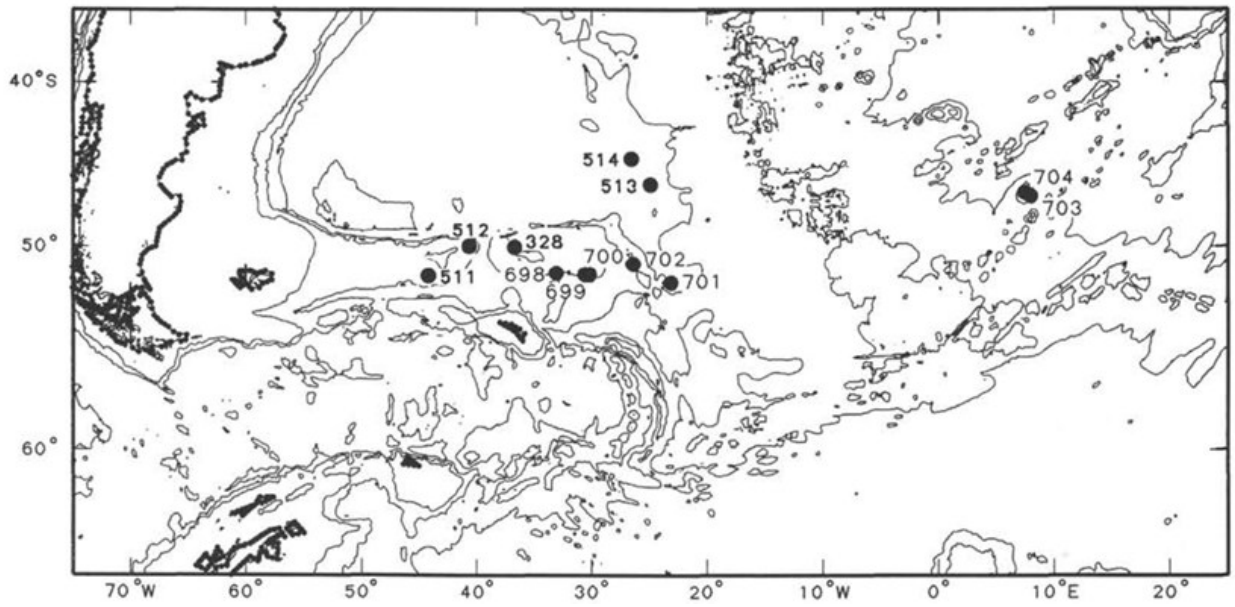

Figure 2.3.: Bathymetic chart of the subantarctic South Atlantic showing the location of Site 702 and other Leg 114 sites. Contour interval 1500 m. (Ciesielski et al. (1988), ODP Initial Reports, Leg 114)

For most of its extent, the Islas Orcadas Rise is mantled by 2 to 3 kilometers of pelagic sediment, which thins progressively toward the flanks, exposing acoustic basement on the outer margins. The sedimentary cover is thickest along the crest and upper western slope, and seismic profiles reveal laterally continuous, undisturbed layering. The eastern and northern flanks display more variable cover, with sediment thickness decreasing sharply and underlying basement features becoming visible. The rise is underlain by oceanic crust formed during the early phases of South Atlantic seafloor spreading, and its tectonic setting is relatively stable with no major post-depositional deformation (Barker & Kennett, 1988).

Tectonic reconstructions of the South Atlantic suggest that the Islas Orcadas Rise and its conjugate feature, the Meteor Rise, were once linked prior to the opening of the South Atlantic Ocean. Prior to rifting, this region was situated adjacent to the southern margin of Africa. The break-up of Gondwana during the Late Jurassic to Early Cretaceous led to progressive spreading between South America and Africa, isolating the Islas Orcadas Rise on the western side of the nascent South Atlantic. The formation of oceanic crust in this area is dated to the Early Cretaceous, and magnetic anomalies support a chronology consistent with early seafloor spreading. The structural

and volcanic evolution of the rise reflects the initial rifting phase and subsequent transition to full oceanic crust accretion (Barker & Kennett, 1988).

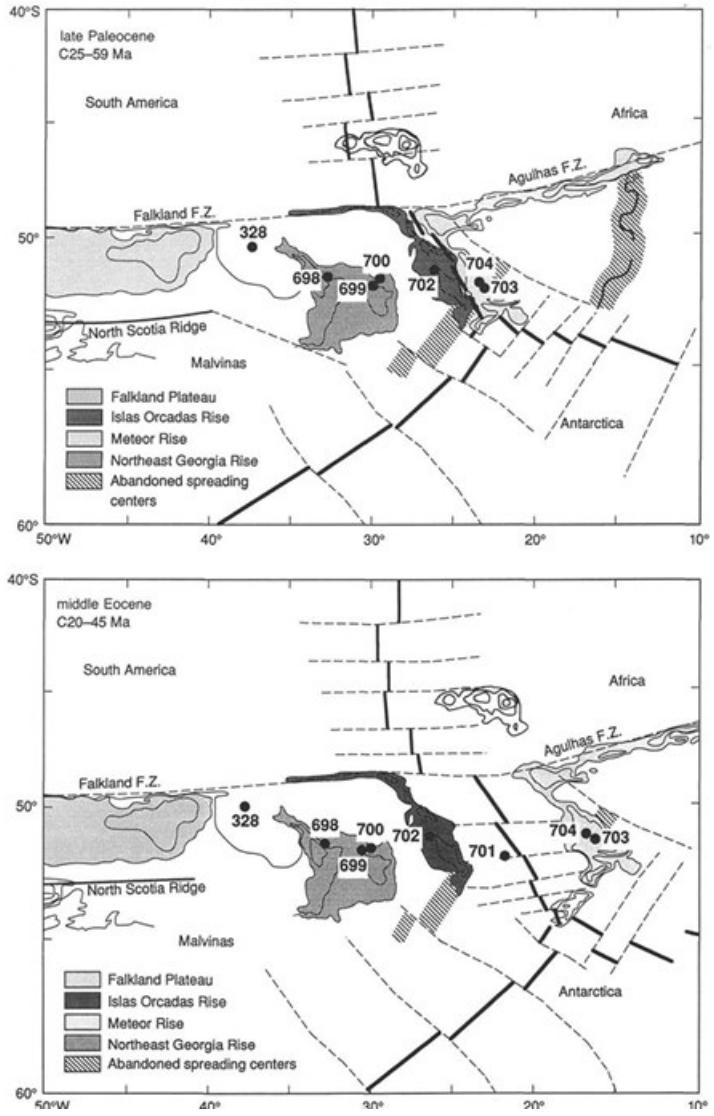

Figure 2.4 Plate tectonic reconstruction of the subantarctic South Atlantic during the late Paleocene (top) and middle Eocene (bottom). The Islas Orcadas Rise and Meteor Rise are shown in their present configuration, along with ODP Leg 114 sites. Spreading-center locations are based on magnetic anomaly data and SEASAT gravity field. Adapted from LaBrecque (1986), in Barker & Kennett (1988).

3. MATERIALS AND METHODS

3.1. Materials: Introduction to Site ODP 702

During Leg 114, four main sites were drilled on the Islas Orcadas Rise: Sites 699, 700, 701, and 702. These sites were strategically positioned along a depth transect to capture variations in sediment accumulation and preservation across water depth and geographic gradients.

Site ODP 702 is located near the crest of the Islas Orcadas Rise, at approximately 50°41.96′S, 27°32.52′W, in the subantarctic South Atlantic. The current water depth at this location is 3364.8 meters. The sediments recovered at this site primarily reflect a pelagic depositional environment influenced by the evolving Antarctic Circumpolar Current and the proximity to the Southern Ocean polar front. The stratigraphy includes calcareous and siliceous oozes interbedded with clay-rich layers, offering an excellent archive for studying Paleogene paleoceanographic and climatic variations (Ciesielski et al., 1988).

Drilling at Site 702 was carried out using the Rotary Core Barrel (RCB) system. Two holes were completed: Hole 702A and Hole 702B. In Hole 702A, drilling reached a total depth of 185.4 meters below sea floor (mbsf) with a core recovery of approximately 84.1%. In Hole 702B, a total of 466.6 mbsf was drilled, with an overall recovery of about 75.3%.

3.2. Lithostratigraphy at Site ODP 702

The sedimentary succession recovered at Site 702 is formally divided into two major lithostratigraphic units, distinguishable by differences in sediment composition, color, degree of lithification, and biogenic content. The studied section spans 294.3 meters below seafloor (mbsf), compiled from Hole 702A (0–185.4 mbsf) and Hole 702B (0–466.6 mbsf, with lithological logging down to 294.3 mbsf). A pronounced unconformity interrupts the sequence, marking a hiatus of approximately 29 million years that separates the upper Neogene–Quaternary siliceous sediments of **Unit I** from the lower Paleogene calcareous deposits of **Unit II**.

Both major units are subdivided into finer subunits based on smear-slide analysis, sedimentary structures, and compositional trends (Ciesielski et al., 1988). The focus of this thesis pertains to **Lithostratigraphic Unit II**, whose detailed subunit division is presented below.

LITHOSTRATIGRAPHIC UNIT II

(22.1 – 294.3 mbsf in Hole 702B; 22.1 – 185.4 mbsf in Hole 702A)

(late Eocene – late Paleocene)

Unit II is a thick calcareous sequence composed predominantly of nannofossil ooze, chalk, and indurated chalk interbedded with chert layers. The sediments are light greenish-gray to white in color and display increasing lithification with depth. Carbonate content ranges from 76% to 95% in the upper sections and decreases to around 63% near the base. This unit offers a continuous and biostratigraphically complete Paleogene record, making it ideal for studying major climatic events such as the Middle Eocene Climatic Optimum (MECO) and the Eocene-Oligocene transition. Three subunits are distinguished.

Subunit IIA

(22.1 – 32.8 mbsf in Hole 702B; 22.1 – 33.0 mbsf in Hole 702A)

Composed of soft, structureless calcareous nannofossil ooze, Subunit IIA has a carbonate content of 76–88%, averaging above 80%. The sediment color is light greenish-gray to white. Microfossil content is dominated by calcareous nannofossils, with rare occurrences of diatoms and foraminifera. Bioturbation is minor to moderate, and the sediment is unlithified. The contact with Subunit IIB is marked by a rapid increase in lithification and appearance of chert.

Subunit IIB

(32.8 – 202.45 mbsf in Hole 702B)

This subunit includes chalk with a high carbonate content of 85% to 95%. The sediments range from pale yellow-gray to white and become increasingly indurated with depth. Chert layers appear below 149 mbsf and increase in frequency downward. Signs of diagenesis, including recrystallization, are present. Bioturbation is moderate, and thin volcanic ash layers are scattered throughout. The transition to Subunit IIC is gradual and marked by increased siliceous content.

Subunit IIC

(202.45 – 294.3 mbsf in Hole 702B)

The deepest subunit consists of highly indurated chalk and silicified limestone, interbedded with frequent chert stringers and nodules. Carbonate content declines gradually from 93% to

approximately 63%. The sediment color varies from light to dark greenish-gray. Lithification is strong, porosity is low, and bulk density is high. This interval preserves the oldest Paleogene sediments at the site and is critical for reconstructing deep-sea carbonate dynamics and early diagenetic processes.

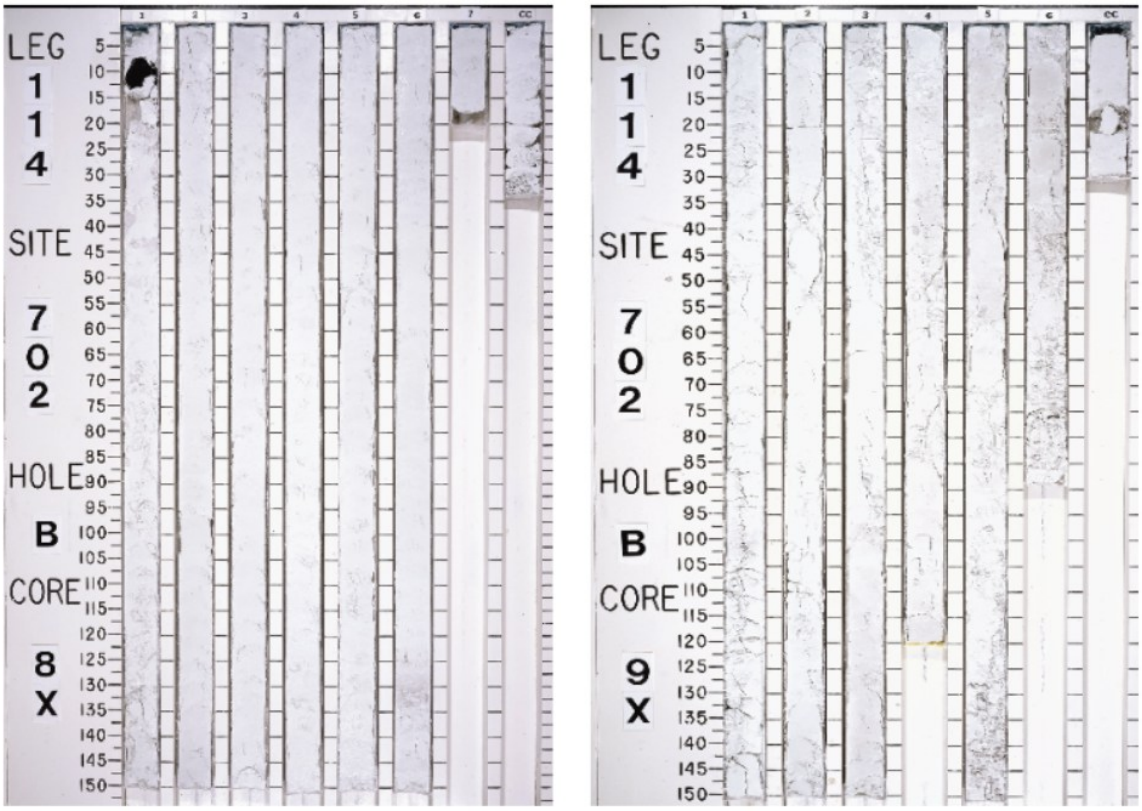

Figure 3.2.: Photographic composite of two sediment cores under study at Site ODP 702B: Core 702B-8X (left) and Core 702B-9X (right). These cores were recovered during ODP Leg 114 using the Extended Core Barrel (XCB) system and correspond to the lower part of Lithostratigraphic Unit II. The cores consist predominantly of Paleogene calcareous nannofossil chalk and indurated chalk, exhibiting increasing lithification and the appearance of chert layers with depth (Ciesielski et al., 1988; ODP Leg 114 Initial Reports, http://www-odp.tamu.edu/publications/114_IR/114TOC.HTM).

3.3. Preliminary data for Site ODP 720

3.3.1. Magnetostratigraphic data

Shipboard paleomagnetic analyses conducted during ODP Leg 114 at Site 702B provided a preliminary magnetostratigraphic framework (Clement & Hailwood, 1991), though the data were limited due to low remanent intensity and incomplete core recovery. To refine this framework, Rivero-Cuesta et al. (2019) performed high-resolution analyses using discrete samples. They confidently identified the C18n.2n–C18r Chron boundary between 70.14 and 74.43 mbsf, offering improved chronological control for the MECO interval. These data support integration of magnetostratigraphy with biostratigraphic and lithologic records in the present study (figure 3.3).

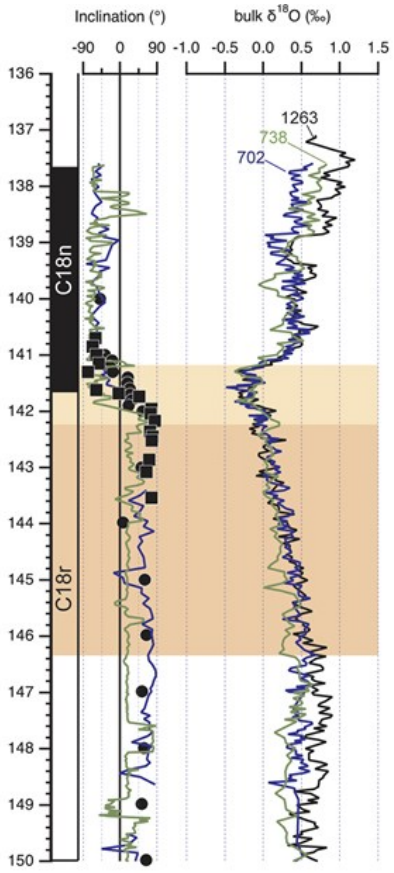

Figure 3.3. Magnetostratigraphic profile of Site ODP 702B showing inclination data and bulk $\delta^{18}O$ records used to constrain the position of the Middle Eocene Chron C18n.2n–C18r boundary (Rivero-Cuesta et al. (2019))

3.3.2. Biostratigraphic data for the interval of interest

Shipboard calcareous nannofossil biostratigraphic data are available for the studied interval at Site ODP 702 (Ciesielski et al., 1988). More recent and refined data are provided by Rivero-Cuesta et al. (2019) and will be compared with the analyses carried out in this thesis.

3.4. Methods

The analysis of calcareous nannofossils from ODP Site 702 was conducted using standard light microscopy techniques at the laboratories of the University of Padova. The methodological framework follows closely that employed in previous studies (e.g., Fornaciari et al., 2007; Agnini et al., 2014).

Smear slides were prepared from selected core samples taken from Holes 702A and 702B, spanning the middle Eocene. The standard smear slide technique was applied, using Norland Optical Adhesive as the mounting medium and coverslips fixed by ultraviolet light. Slides were examined under a Leica DM750-P polarizing microscope at 1000× magnification under both cross-polarized and transmitted light (Bown, 1998).

Quantitative counts were performed on each slide, with a minimum of 300 specimens counted per sample. For stratigraphically important taxa, additional counts were conducted within a defined area (in mm^2), following the method described by Backman and Shackleton (1983). This approach was adopted because many of these taxa are rare, and extending the counting beyond the initial 300 specimens helped to obtain a more continuous and reliable abundance signal.

Taxonomic identification in this study followed the framework of Perch-Nielsen (1985) and Agnini et al. (2014), with additional reference to the updated classifications available in Nannotax (nannotax.org). Species identification also considered the site-specific taxonomy provided by Rivero-Cuesta et al. (2019).

Biostratigraphic zonation was established by identifying calcareous nannofossil biohorizons (e.g., first and last occurrences of key taxa), which were then used to define the boundaries of biozones following the schemes of Martini (1971), Okada and Bukry (1980), and the refined Paleogene Superzone framework by Agnini et al. (2014).

Assemblage data were used to recognize key calcareous nannofossil biohorizons, specifically the local base or top occurrences of stratigraphically important taxa, as defined in Martini (1971), Okada and Bukry (1980), and Agnini et al. (2014). These biohorizons were used to assign biozones only when reliably identified. In intervals where marker species were absent or preservation was too poor to support confident identification, no formal biozone boundaries were defined, though changes in assemblage composition were noted for stratigraphic context. All data were compiled into spreadsheets and species abundance pattern for comparison with global reference records.

Figure 3.4: Laboratory workflow for calcareous nannofossil analysis. From left to right: sample preparation under fume hood with precision scale and tools; observation under a Zeiss polarizing microscope; prepared smear slides organized and labeled for analysis. Photos taken at the Department of Geosciences, University of Padova.

4. INTRODUCTION TO CALCAREOUS NANNOFOSSIL BIOSTRATIGRAPHY AND BIOCHRONOLOGY

4.1. Definition and reliability of a biohorizon

According to the *International Guide to Stratigraphic Nomenclature* (Salvador, 1994), a **biohorizon** is a clearly recognizable change in fossil content within a sedimentary succession. It represents a distinct biostratigraphic surface that can be identified based on the first or last occurrence, abundance peak, or morphological variation of specific fossil taxa.

Biostratigraphic events that define biohorizons can be driven by two principal mechanisms:

- **Evolutionary processes** (non-repetitive), such as the true appearance (origination) or disappearance (extinction) of taxa. These events represent irreversible biological changes and are most valuable for global correlations.
- **Environmental changes** (repetitive), which can include migration, ecological exclusion, or fluctuations in abundance caused by local or regional factors. These may result in temporary absences or morphotype variations within a given stratigraphic interval.

In biostratigraphy, it is essential to assess the **reliability** of a biohorizon before using it for correlation. A reliable biostratigraphic event must display consistent **relative ordering** (ranking) and **temporal spacing** when compared across multiple stratigraphic successions and between different studies. Its recognition should be replicable, objective, and as independent of local paleoenvironmental conditions as possible.

The primary criteria used to evaluate the reliability of a biohorizon include:

- **Ease of recognition** of the species that defines the event (clear diagnostic morphologic features and unambiguous taxonomy);
- **Continuous abundance pattern** of the marker species especially at the event level, which facilitates detection of the biohorizon;
- **widespread geographic distribution** across different basins and depositional settings;

- **Possibility of reworking** unfortunately, for nannofossils, due to their abundance and small size, this can be a problem, especially in certain depositional settings. In such contexts, the reliability is potentially lower.
- **Preservation potential** that allows specimens of the taxon used to be present even in sediments affected by dissolution or recrystallization. **Correlatability**, allowing for confident identification in both local and regional settings
- **Synchroneity** — good synchroneity means that the event is recorded in different areas with good temporal alignment, thus allowing for correlations between regions and/or across different basins.

When these criteria are met, the biohorizon can be considered a robust and valuable stratigraphic marker (These criteria are widely accepted and are described in detail by Agnini et al. (2014).) It serves as a foundation for high-resolution correlations and supports the development of accurate biostratigraphic frameworks.

4.1.1. Bio-horizons used

In this thesis, we adopt the updated and standardized nomenclature for biostratigraphic events proposed by **Backman et al. (2012)**, which aims to reduce ambiguity and improve clarity in the description of biostratigraphic datums. Traditional acronyms such as FO (First Occurrence) and LO (Last Occurrence), as well as the alternatively used LO (Lowest Occurrence) and HO (Highest Occurrence), often carry conflicting meanings in the literature. To avoid this confusion, the following unambiguous notations are employed:

- **B** = Base of a taxon (i.e., the lowest stratigraphic occurrence)
- **Bc** = Base of common and continuous occurrence
- **T** = Top of a taxon (i.e., the highest stratigraphic occurrence)
- **Tc** = Top of common and continuous occurrence

In this thesis, the biohorizons used are defined using the four types mentioned above. The positions of individual biohorizons are considered as midpoints between two successive samples. For example, a base event **B(x)** for taxon *x* is placed between the sample in which it first appears and the preceding sample in which it is absent. Similarly, **T(x)** marks the midpoint between last sample

in which taxon *x* is present and the immediately overlying sample where the taxon is no longer present.

This standardized approach facilitates a more consistent identification of bioevents, both within and across sedimentary sequences, and supports more robust stratigraphic correlations.

4.2. Paleogene calcareous nannofossil biozonation: an Introduction

The traditional/standard biozonation schemes for the middle and late Eocene are those proposed by Martini (1971) and Okada & Bukry (1980). These schemes build upon the pioneering work of Hay et al. (1967), Bramlette & Wilcoxon (1967), Roth (1970, 1973), Roth et al. (1970), and Bukry (1973, 1975).

Within the time interval analyzed in this thesis, Martini (1971) designates biozones using the prefix "NP" (Nannoplankton Paleogene), arranging them in a progressive numerical sequence. An alternative coding system, also covering the entire Cenozoic, was introduced by Bukry (1973), primarily based on his studies conducted within the framework of the Deep-Sea Drilling Project (DSDP) (Bukry, 1970, 1971, 1973, 1975a).

Building on this work, Okada & Bukry published a revised version of the earlier biozonation in 1980. In their scheme, biozones are labeled with the prefix "CP" (Coccolith Paleogene), followed by letters a, b, or c to identify subzones, and a sequential number.

More recently, Fornaciari et al. (2010) published a mid-latitude calcareous nannofossil biozonation for the middle to late Eocene transition, which represents an update of the scheme previously proposed by Catanzariti et al. (1997). In this case, the coding system uses the prefix "MPN" (Mediterranean Paleogene Nannoplankton), followed by a sequential number. Subzones are indicated by an uppercase letter (A, B, C), with additional subdivisions marked by lowercase letters (a, b, c) when necessary.

Finally, and more recently, a Paleogene biozonation specifically designed for low- and mid-latitude regions was proposed by Agnini et al. (2014). In this scheme, the coding system uses the prefix "CN" (Calcareous Nannofossil), followed by a letter indicating the geologic stage (e.g., "E" for Eocene), and a progressive number corresponding to progressively younger biozones. This new

biozonation was prompted by the observation that several biohorizons included in previous schemes had proven to be unreliable.

These four biozonation schemes will therefore constitute the biostratigraphic framework for this Master's thesis.

In practical application, the identification of nannofossil biozones is based on the recognition of biostratigraphic events within the examined samples (e.g., Base, Top), which are then used to define biozone boundaries. These zones form the foundation for biostratigraphic framework of ODP Site 702 in the study interval.

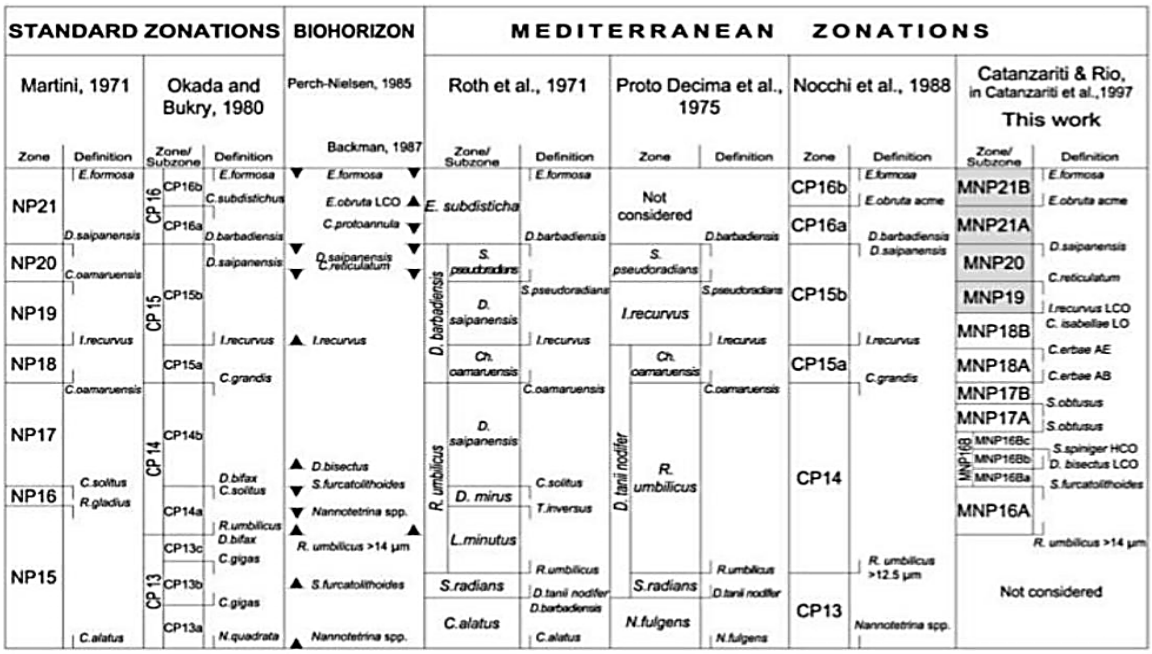

Figure 4.2.1: Comparative chart showing calcareous nannofossil biozonation schemes. Standard schemes (Martini, 1971; Okada & Bukry, 1980), biohorizons (Backman, 1987; Perch-Nielsen, 1985), Mediterranean schemes (Roth et al., 1971; Proto Decima et al., 1975; Nocchi et al., 1988), and the updated MNP zonation from Catanzariti & Rio (1997) are aligned for reference. This study follows the MNP biozonation framework shown in the column labeled "This work," as adopted in Fornaciari et al. (2020).

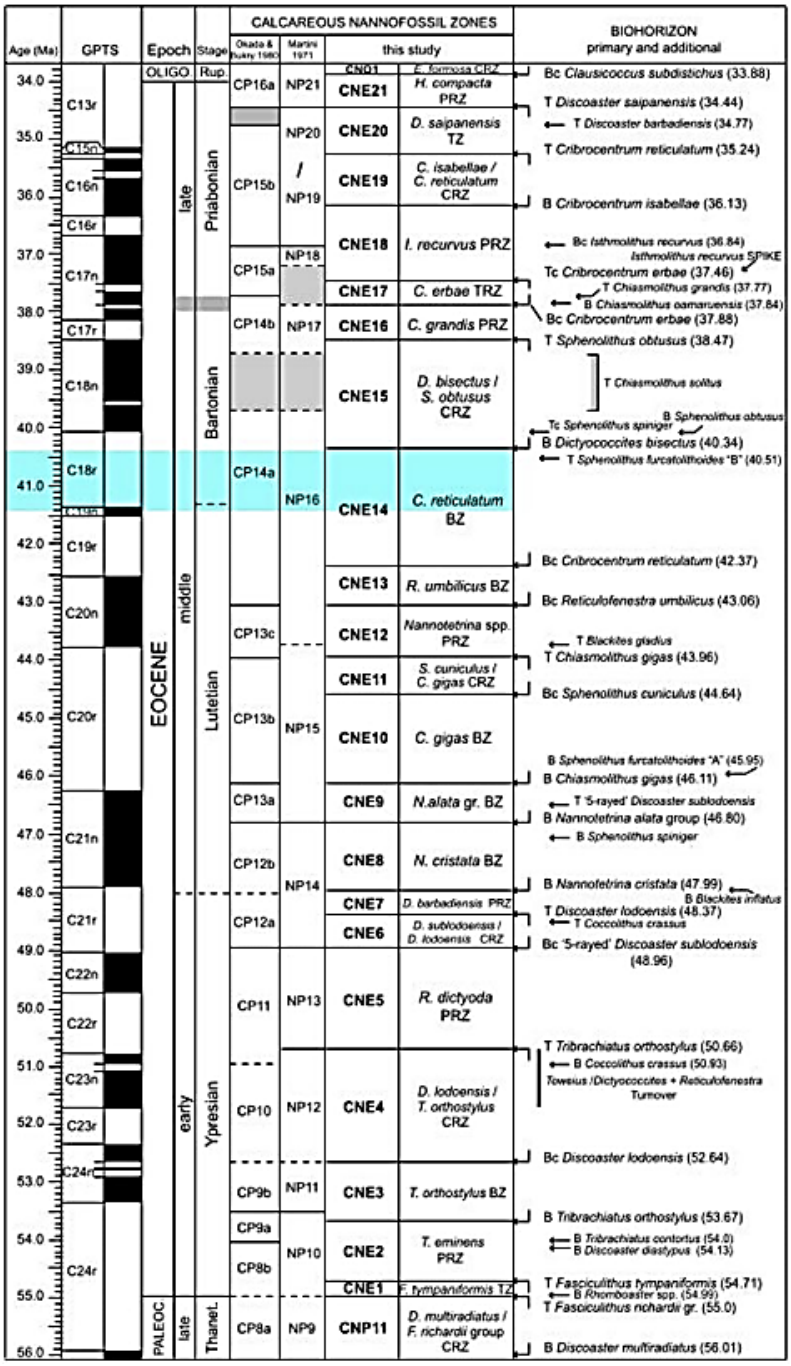

Figure 4.2: The CN biozones and calcareous nannofossil biohorizons proposed for the Eocene by Agnini et al. (2014) are reported alongside the biozoning schemes of Martini (1971) and Okada & Bukry (1980). The Geomagnetic Polarity Time Scale (GPTS) follows Cande & Kent (1995) and Pälike et al. (2006). The grey bands represent the uncertainty in defining chronostratigraphic and biozone boundaries, while the blue box highlights the interval considered in this thesis based on the recognized biohorizons (modified from Agnini et al., 2014).

4.2.1. Notes on biochronology

Biostratigraphy is the branch of stratigraphy that establishes the relative ages of sedimentary rocks based on their fossil content. It primarily relies on the identification of biostratigraphic events, or biohorizons, which are defined by the first or last occurrences, or significant changes, in fossil taxa within a sequence. These events may be related to evolutionary originations or extinctions, but can also reflect ecological or taphonomic factors (Murphy et al., 2008).

Biochronology, in contrast, refers to the time-based framework developed by integrating biostratigraphic data with absolute geochronological information. Its goal is to assign ages to bioevents and enable correlations across regions and depositional settings. Unlike biostratigraphy, which is based on rock stratification, biochronology emphasizes temporal equivalence of fossil events regardless of lithology (Murphy et al., 2008).

For the Paleogene, multiple time scales have been proposed, each based on different calibration techniques such as radiometric dating, astronomical tuning, or magnetostratigraphy. These include widely used references such as Cande and Kent (1995), Lourens et al. (2004), and Pälike et al. (2006), among others. As a result, the absolute ages assigned to key bioevents or polarity chrons can vary slightly among them. To ensure consistency in age comparisons, it is essential to adopt a single time scale and recalibrate other data accordingly. This recalibration process is particularly critical when integrating bio- and magnetostratigraphic data across different studies and basins.

In this thesis, the calibration of calcareous nannofossil biohorizons is based on the biochronological synthesis by Agnini et al. (2014), which integrates magnetostratigraphic and biostratigraphic data and provides updated numerical ages for key bioevents using the GTS 2012 framework. This calibration enables comparison with previously published zonations (e.g., Martini, 1971; Okada & Bukry, 1980) while maintaining consistency with the most recent timescale revisions.

Importantly, while the position of a biohorizon within a given magnetic polarity chron (e.g., C18r, C18nr) remains fixed, the absolute age of the base and top and its duration of the Chron—and thus of the biohorizon—can vary slightly depending on the adopted GTS. Therefore, care is required when comparing age assignments across different studies.

5. RESULTS AND DISCUSSION

5.1. General characteristics of the calcareous nannofossil assemblage at Site ODP 702 during the Middle Eocene

At Site ODP 702, located on the central part of the Islas Orcadas Rise in the South Atlantic Ocean, the calcareous nannofossil assemblages recovered from Hole 702B are generally abundant and moderately to well-preserved throughout the middle Eocene interval. Preservation tends to be better in the chalk-dominated intervals, especially between ~33 and 202 meters below seafloor (mbsf), where carbonate content consistently exceeds 85% (Ciesielski et al., 1988). This well-lithified and relatively continuous section provides a robust sedimentary archive for paleoecological and biostratigraphic interpretation.

The dominant taxonomic component in the studied assemblages is the genus *Reticulofenestra*, which appears consistently abundant across the interval. Other genera, such as *Coccolithus*, *Discoaster*, *Sphenolithus*, and *Ericsonia*, are frequently present and often exhibit notable abundance changes that reflect paleoenvironmental variability. Accessory taxa, including *Chiasmolithus*, *Zygrablithus*, *Cyclicargolithus*, *Cribrocentrum*, and *Dictyococcites*, also contribute to the assemblage but are generally less common. Several stratigraphically important species among these genera provide valuable biohorizons for age calibration.

Following the astronomically tuned age model developed by Rivero-Cuesta et al. (2019) and based on the correlation of high-resolution bulk $\delta^{13}C$ records between Sites 702, 738, and 1263, the section analyzed at Site 702 spans a ~300 kyr interval from approximately 40.51 to 40.21 Ma, encompassing the onset, peak, and recovery phases of the Middle Eocene Climatic Optimum (MECO). The biostratigraphic framework at this site is further constrained by magnetostratigraphic data indicating the C18r–C18n.2n reversal boundary, which occurs within the MECO peak interval.

Calcareous nannofossil data from Site 702 also reveal key paleoecological changes across the MECO. In particular, a pronounced increase in warm-water taxa and a biogeographical shift

toward higher latitudes are interpreted as a response to rising sea-surface temperatures. These findings are consistent with the global ecological trends documented during the MECO in other ocean basins (e.g., Villa et al., 2008; Agnini et al., 2014).

The biostratigraphic data collected from Site 702 have been compared with published zonations (Martini, 1971; Okada & Bukry, 1980; Agnini et al., 2014) and integrated with both stable isotope ($\delta^{18}O$ and $\delta^{13}C$) and magnetostratigraphic records (Clement & Hailwood, 1991; Rivero-Cuesta et al., 2019). This multiproxy approach allows for high-resolution correlation of the MECO interval and improves our understanding of the timing, duration, and paleoceanographic consequences of this climatic perturbation at southern high latitudes.

5.2. Biostratigraphy and biochronology of calcareous nannofossils at Site ODP 702

Biostratigraphy is the branch of stratigraphy that assigns relative ages to sedimentary layers based on their paleontological content, particularly the recognition of biohorizons or bioevents. Biochronology differs in that it aims to estimate or calibrate absolute ages for these events, such as first and last occurrences of key taxa (e.g., FAD and LAD; Agnini et al., 2014). A single biochronological datum is often not sufficient to assess the reliability of a given biohorizon, as calibrations can vary across regions and depositional settings.

5.2.1. Biostratigraphic results

5.2.1.1. The biohorizons of standard biozoning

The following paragraphs describe the biohorizons used in the "standard" biostratigraphic schemes (Martini, 1971; Okada & Bukry, 1980) that have been recognized within the studied interval at ODP Site 702. For each event recorded at ODP Site 702, a position in meters below seafloor (mbsf) is provided. The relative position among the bioevents is discussed with respect to the available literature data, specifically the biozonation proposed by Agnini et al. (2014) and the results from Rivero-Cuesta et al. (2019) at the same site. The position of the biohorizons is reported in Table 5.1. For each sample, metadata such as Site, Hole, Core, Top Interval, Bottom Interval, Top Depth (mbsf), and corresponding mean age are provided.

Top *Reticulofenestra umbilicus* (Top Zone CP14a)

The base of Subzone CP14a (Okada & Bukry, 1980), defined by the first occurrence of *Reticulofenestra umbilicus* (>14 μm), is widely used to approximate the base of Zone NP16 in the scheme of Martini (1971). This bioevent also corresponds to the base of Zone CNE13 according to the Paleogene zonation proposed by Agnini et al. (2014).

Reticulofenestra umbilicus shows a rare and discontinuous distribution in the lower part of the studied interval at Site 702 B. Although it is recorded in Sample 702B-8H-4W,130 cm (Top depth: 69.00 mbsf), it is absent in several shallower levels, making its last consistent occurrence difficult to pinpoint based solely on this dataset. However, when compared with the results of Rivero-Cuesta et al. (2019), who placed the base of the studied succession within Zone CNE14, it can be inferred that *R. umbilicus* is present from the very base of the section.

Base *Chiasmolithus solitus* (Base Zone NP17)

The base of Zone NP17 (Martini, 1971), defined by the Base, falls within Subzone CP14b of Okada & Bukry (1980) and corresponds to the middle part of Zone CNE14 as shown in Figure 8 of the Paleogene zonation by Agnini et al. (2014). The Top of *Chiasmolithus* is a diachronous event, especially when comparing high with mid- to low-latitude records. In any case, it is consistently reported as occurring after the Middle Eocene Climatic Optimum (MECO). The abundance data for *C. solitus* obtained in this thesis once again shows a discontinuous pattern. However, when comparing our results with those of Rivero-Cuesta et al. (2019), it becomes evident that this species is nonetheless present throughout the section, and its disappearance is not recorded within the studied interval at Site 702.

5.2.1.2. Additional Biohorizons

The biohorizons used in standard zonations (Martini, 1971; Okada & Bukry, 1980) classify the investigated interval at Hole 702B within Zone NP16 and Subzone CP14a. However, in order to enhance the biostratigraphic resolution achieved so far, additional biohorizons have been applied based on schemes proposed by Fornaciari et al. (2010), Agnini et al. (2014), and validated by more recent high-resolution studies such as Rivero-Cuesta et al. (2019). These events are particularly

useful for resolving the stratigraphy of the middle Eocene Climatic Optimum (MECO) and allow for a more refined correlation with regional and global frameworks. The following paragraphs describe the position and behavior of these additional bioevents in the succession at Hole 702B, using semi-quantitative data obtained in this thesis and comparing them with the literature.

Base *Cribrocentrum reticulatum* (base Zone CNE14)

The biostratigraphic scheme of Agnini et al. (2014) uses the Base common and continuous (Bc) of *Cribrocentrum reticulatum* to define the base of Zone CNE14. This biozone corresponds approximately to the central part of Zone NP16 (Martini, 1971) and Subzone CP14a (Okada & Bukry, 1980). The calibration of this event against the Geomagnetic Polarity Time Scale (GPTS) remains somewhat debated: Berggren et al. (1995) placed the Base of this species within Chron C19n, while Wei & Wise (1990) documented its appearance only after the base of Chron C18n.2n. More recently, Agnini et al. (2014) estimated the Base of *C. reticulatum* at 42.37 Ma, within Chron C19r.

Chiasmolithus reticulatus is very rare and discontinuous within the studied interval, in agreement with the data reported by Rivero-Cuesta et al. (2019). Furthermore, according to Pea (2011), the first occurrence of this species is documented below the base of the interval analyzed in this thesis. The oldest sample examined in this study already falls within Zone CNE14.

Top Sphenolithus furcatolithoides (base Subzone MNP16B)

The Top of *Sphenolithus furcatolithoides* defines the base of Subzone MNP16B, as proposed by Fornaciari et al. (2010). This subzone corresponds stratigraphically to the upper part of Zone NP17 (Martini, 1971) and Subzone CP14b (Okada & Bukry, 1980), and is positioned in the higher portion of Zone CNE14 in the scheme of Agnini et al. (2014). Earlier, Perch-Nielsen (1985) also suggested this taxon's disappearance as a potential biohorizon for delineating the base of NP17.

In the present study at Site 702, *S. furcatolithoides* was not observed in any of the investigated samples. Its absence may reflect genuine paleoenvironmental exclusion, poor preservation conditions, or a position outside its known stratigraphic range. Rivero-Cuesta et al. (2019) reported

the finding of a single specimen of *S. furcatolithoides* at 79.40 mbsf. This isolated occurrence does not allow for a precise placement of the Top of the species. However, the specimen lies — as expected — between the base of *Reticulofenestra umbilicus* and the first appearance of *Dictyococcites bisectus*. As in Rivero-Cuesta et al. (2019), this biohorizon cannot be precisely placed in the present study. Nonetheless, its validity at low to mid-latitudes is confirmed, and the position of Site 702 at mid- to high-latitudes likely explains the ecological exclusion of warm-water taxa such as *S. furcatolithoides*.

Base *Dictyococcites bisectus* (base Subzone CNE15)

The base of Zone CNE15 in the calcareous nannoplankton zonation proposed by Agnini et al. (2014) is marked by the Base (B) of *Dictyococcites bisectus*. This event lies above the base of *Cribrocentrum reticulatum* (base of Zone CNE14) and provides an important refinement for middle Eocene stratigraphy. Although *D. bisectus* is not part of the standard biostratigraphic schemes of Martini (1971) or Okada & Bukry (1980), it has been increasingly adopted in recent literature to improve the resolution.

According to Agnini et al. (2014), the Base of *D. bisectus* defines the Base of Zone CNE15 and is estimated to occur within Chron C18r, with an approximate age of 40.4Ma (Agnini et al., 2014), roughly corresponding with the onset of the negative $\delta^{18}O$ shift. Rivero-Cuesta et al. (2019) identified this event at Site 702 as one of the key stratigraphic markers across the MECO interval, where it consistently occurs above the Base of *Cribrocentrum reticulatum*.

In the present study at Site 702B, the Base of *D. bisectus* is recorded in Sample 702B-8H-5W, 150 cm (Top depth 70.80 mbsf), where the species is documented in low but distinct numbers. It continues to occur in subsequent samples, including 702B-8H-6W, 10 cm and 50 cm (Top depths 70.9–71.3 mbsf), indicating a continuous presence. Preservation is moderate, and the specimens were clearly identifiable under cross-polarized light without significant evidence of reworking.

At Site 702, this taxon shows a relatively rare occurrence, which, as suggested by Rivero-Cuesta et al. (2019), is likely due to its temperate affinity (Haq & Lohmann, 1976; Villa et al., 2008; Wei & Wise, 1990). These same authors report a relatively continuous presence of this taxon, which allows the base of the CNE15 Zone to be defined. In the data presented in this thesis, the occurrence

of this species appears to be even rarer, yet it is broadly consistent with the available literature, which has been used here to place the base of Zone CNE15.

Top *Sphenolithus spiniger* (base Subzone MNP17A)

The Top of *Sphenolithus spiniger* marks a key bioevent that defines the base of Subzone MNP17A, as proposed by Fornaciari et al. (2010). This taxon, a warm-water sphenolith, is not included in the standard schemes of Martini (1971) or Okada & Bukry (1980), but has been widely adopted in recent biostratigraphic frameworks. According to Rivero-Cuesta et al. (2019), *Sphenolithus spiniger* is virtually absent in the lower part of the studied interval at Site 702, but occurs rarely and continuously between ~73.05 and 70.80 mbsf, disappearing just above this interval. This disappearance has also been documented at other low- to middle-latitude sites, including Sites 1051, 1052, 1263, and Alano (Italy) (Fornaciari et al., 2010; Toffanin et al., 2011; Agnini et al., 2014).

In the present thesis at Site 702, *S. spiniger* was recorded only once, in Sample 702B-9H-1W, 40 cm; Top depth 73.00 mbsf. The species is absent in all other investigated samples. Its rare and uneven occurrence reflects the ecological exclusion and very low abundance reported by Rivero-Cuesta et al. (2019). The specimen identified is moderately preserved, with no apparent evidence of reworking or contamination, though its singular presence prevents the placement of the biohorizon associated with the disappearance of this species.

Top *Discoaster saipanensis* (upper part of Zone CNE14)

Although the disappearance (top occurrence) of *Discoaster saipanensis* has been used as a secondary biohorizon in high-resolution schemes such as those proposed by Fornaciari et al. (2010) and Agnini et al. (2014), its biostratigraphic utility remains limited due to its rare and discontinuous distribution, especially outside tropical to subtropical settings. As a warm-water taxon, the absence of *D. saipanensis* in many temperate sections—including portions of Site 702—may reflect paleoecological constraints rather than true extinction events.

In the present study, *D. saipanensis* was identified only once, in Sample 702B-8H-6W, 50 cm (Top depth: 71.30 mbsf), where it was found as a rare but recognizable specimen under cross-polarized light. No additional occurrences were recorded in the surrounding samples above or below. Given this isolated occurrence and the absence of consistent recurrence, no definitive biohorizon associated with this species can be reliably established in this section.

Nevertheless, the depth at which this single occurrence was recorded aligns with the stratigraphic interval proposed by Rivero-Cuesta et al. (2019) for the decline of *D. saipanensis* near the end of the MECO. Therefore, while not considered a primary marker in this study, its presence may support broader paleoecological interpretations when integrated with regional datasets.

5.2.1.3 Biostratigraphic classification of the studied section

The simultaneous presence of *Reticulofenestra umbilicus* and *Chiasmolithus solitus* in the analyzed samples indicates that the studied succession at Site 702 can be attributed to Zone NP16 of Martini (1971). In parallel, the absence of *B. gladius* and the confirmed occurrence of *C. solitus* support classification within Subzone CP14a of Okada & Bukry (1980).

Following the calcareous nannoplankton zonation proposed by Agnini et al. (2014), the section is assigned to the CNE14 Zone, based on the presence of *Cribrocentrum reticulatum* and the base of *Dictyococcites bisectus*, which defines the transition to Subzone CNE15. However, since *D. bisectus* appears in the lower part of the studied interval (Sample 702B-8H-5W, 150 cm), most of the section can be attributed to the upper part of Zone CNE14, with only the basal portion of Subzone CNE15 possibly represented.

Additionally, the rare occurrence and subsequent disappearance of *Sphenolithus spiniger* near 73.00 mbsf corresponds to the base of Subzone MNP17A, as defined by Fornaciari et al. (2010). The presence of *Discoaster barbadiensis* and *Discoaster saipanensis* further supports the placement of the succession within the middle to upper part of Zone CNE14, consistent with the MECO interval as documented by Rivero-Cuesta et al. (2019).

Finally, the absence of *Sphenolithus furcatolithoides* and the limited occurrence of *Dictyococcites hesslandii* confirm that the section lies below Subzone MNP16B, and within the MNP16A–

MNP17A interval, reinforcing the attribution of the succession to a late CNE14–early CNE15 age, spanning the middle Eocene climatic optimum at Site 702.

5.3 Calcareous nannofossil biochronology at Site ODP 702

5.3.1 Age model

The ages of calcareous nannofossil biohorizons at ODP Site 702 were calculated using two different age models. The first model is based on magnetostratigraphic calibrations derived from the GPTS framework (Cande & Kent, 1995), as applied by Edgar et al. (2010). The second is a cyclostratigraphic model developed by Westerhold & Röhl (2013) through orbital tuning of $\delta^{13}C$ and $\delta^{18}O$ records, and specifically adapted to Site 702B by Rivero-Cuesta et al. (2019).

- Model I (Edgar et al., 2010)

Following the magnetostratigraphic framework proposed by Edgar et al. (2010), and based on GPTS calibrations by Cande & Kent (1995), the studied interval at Site 702B—from Sample 702B-9H-2W, 40 cm (75.10 mbsf) to 702B-8H-4W, 50 cm (71.30 mbsf)—would correspond to a stratigraphic span between the base of Chron C18r (41.26 Ma) and the base of Subchron C18n.2n (40.13 Ma). This represents a duration of approximately 1.13 million years. Under this model, the MECO (Middle Eocene Climatic Optimum), which spans ~40.6 to 40.1 Ma (Bohaty et al., 2009), would be captured from its onset to the late stages of its main warming phase.

- Model II (Westerhold & Röhl, 2013)

According to the second model, developed by Westerhold & Röhl (2013) and directly applied to Site 702B by Rivero-Cuesta et al. (2019), the same sedimentary interval is constrained using a high-resolution cyclostratigraphic approach. This model is based on the tuning of carbon and oxygen isotope records to orbital eccentricity cycles and anchored to the astronomically calibrated time scale at Site 1263 (Walvis Ridge, South Atlantic). Based on this framework, the succession from Sample 702B-9H-2W, 40 cm to 702B-8H-4W, 50 cm spans from ~40.62 Ma to ~39.73 Ma,

for a total duration of approximately 0.89 million years. This interval includes the late part of Chron C19n, the full extent of Chron C18r, and reaches into the lower part of Subchron C18n.2n.

Application to the studied interval

The results from both models are shown in the supplementary figures and tables of Rivero-Cuesta et al. (2019) (e.g., Figures S1, S5–S6; Table S4). Although both models provide a useful temporal framework, Model II allows for greater stratigraphic precision and better alignment with bioevents observed at Site 702. For instance, the Top of *Sphenolithus furcatolithoides* (at 74.58 mbsf) and the Base of *Dictyococcites bisectus* (>10 μm; at 73.63 mbsf) yield ages of ~40.18 Ma and ~39.89 Ma respectively when calibrated using Model II, consistent with published literature (e.g., Fornaciari et al., 2010; Agnini et al., 2014). In contrast, Model I results in broader and less constrained estimates that do not fully reflect the site-specific sedimentation pattern.

Although both approaches have intrinsic limitations, they are grounded in solid stratigraphic frameworks. For this reason, both age models will be referenced in the discussion where relevant. However, given its higher resolution and local calibration, Model II is adopted as the preferred framework for interpreting the biochronology and timing of the MECO at Site 702.

Top *Sphenolithus furcatolithoides*

At ODP Site 702, the last occurrence of *Sphenolithus furcatolithoides* is recorded in Sample 702B-9H-2W, 40 cm (75.10 mbsf). Based on the astrochronologically tuned age model by Rivero-Cuesta et al. (2019), this datum is calibrated at approximately 40.00 Ma, corresponding to the early MECO phase. Using the magnetostratigraphic model by Edgar et al. (2010), this same biohorizon would be placed at around 40.53 Ma, in agreement with earlier literature estimates (Agnini et al., 2014; Fornaciari et al., 2010).

The calibration obtained from Model II (Westerhold & Röhl, 2013; Rivero-Cuesta et al., 2019) aligns with the bulk carbonate isotope excursion marking the onset of the MECO and is therefore preferred in this study. This calibration is consistent with other sites such as ODP 1052 (40.38 Ma; Fornaciari et al., 2010), although minor diachroneity cannot be excluded.

Base *Dictyococcites bisectus*

The first common occurrence of *Dictyococcites bisectus* (>10 μm) is recorded in Sample 702B-8H-4W, 50 cm (71.30 mbsf), toward the top of the studied interval. According to the tuned age model by Rivero-Cuesta et al. (2019), this biohorizon is assigned an age of approximately 39.73 Ma. In contrast, the magnetostratigraphic calibration by Edgar et al. (2010) would place it closer to 40.15 Ma, which is earlier than observed at this site.

Given the high-resolution tuning of the isotopic and magnetic data in Rivero-Cuesta et al. (2019) and the stratigraphic consistency of the appearance of *D. bisectus* at other Atlantic sites (e.g., Fornaciari et al., 2010), we consider the 39.73 Ma estimate as more reliable. The appearance of this taxon near the paroxysmal MECO stage further supports its biochronological utility in this interval.

Top *Discoaster saipanensis*

At ODP Site 702, *Discoaster saipanensis* is last observed in Sample 702B-8H-5W, 40 cm (71.80 mbsf). Based on the astrochronological tuning from Rivero-Cuesta et al. (2019), this occurrence is calibrated at approximately 39.83 Ma, shortly after the peak of the MECO. According to Model I (Edgar et al., 2010), the same depth would fall near 40.10 Ma, which is slightly older than the cyclostratigraphic estimate.

In other Atlantic sections, the top of *D. saipanensis* has been variably placed, and some diachroneity has been reported (Agnini et al., 2014). At Site 702, the calibration using Model II is in better agreement with the regional stratigraphic trends and isotope excursions, and is thus considered more robust for this horizon.

Base *Dictyococcites aff. bisectus*

The first continuous occurrence of *Dictyococcites aff. bisectus* (<10 μm) at Site 702 is recorded in Sample 702B-8H-5W, 20 cm (71.60 mbsf). This is dated to approximately 39.87 Ma using the astrochronologic model. Under the magnetostratigraphic framework of Edgar et al. (2010), this would correspond to approximately 40.10–40.20 Ma.

This species has been used as a reliable marker in high-resolution biostratigraphic schemes (e.g., Agnini et al., 2014; Fornaciari et al., 2010), and its first appearance in the post-MECO phase at Site 702 is consistent with patterns observed in other South Atlantic and equatorial Atlantic sites.

Top *Dictyococcites hesslandii*

Dictyococcites hesslandii becomes rare and eventually disappears in Sample 702B-8H-5W, 20 cm (71.60 mbsf), the same level where *D. aff. bisectus* appears. Using the tuned age model, this event is dated to ~39.87 Ma, suggesting a closely timed turnover in the assemblage near the end of the MECO recovery phase.

This matches the trend observed at nearby Site 1263, where the top of *D. hesslandii* coincides with significant isotopic recovery (Westerhold & Röhl, 2013). Based on Model I, this event would have occurred slightly earlier (~40.14 Ma), but the Model II calibration fits better with the biotic and geochemical signals at Site 702.

Based on the calcareous nannofossil biohorizons identified in the studied interval at Site 702, the cyclostratigraphic framework of Model II (Westerhold & Röhl, 2013; adapted by Rivero-Cuesta et al., 2019) provides a more coherent and site-specific age model than the global magnetostratigraphic scheme of Model I (Edgar et al., 2010). In particular, the calibration of key events such as the Top of *Sphenolithus furcatolithoides* and the *Base of Dictyococcites aff. bisectus* align closely with known paleoceanographic changes across the MECO and exhibit consistent spacing and ordering within the local $\delta^{13}C$ and $\delta^{18}O$ isotope stratigraphy.

Moreover, the clear separation between the extinction of *S. furcatolithoides* and the appearance of *D. aff. bisectus*, estimated at ~100 kyr, mirrors patterns documented at other Atlantic sites such as ODP 1263 and 1260, reinforcing the reliability of the astrochronologically tuned age model. In contrast, the application of Model I yields slightly older ages for the same events and compresses biostratigraphic spacing, which is less compatible with the observed sedimentary and isotopic cyclicity at Site 702.

Given the high-resolution tuning of the benthic and bulk isotope records to the La2004 orbital solution and the direct transfer of tie-points from Site 1263 to Site 702B (Rivero-Cuesta et al., 2019), Model II enables a more refined integration of paleoenvironmental signals and calcareous nannofossil turnover. Therefore, Model II is adopted as the primary reference for age calibration in this study, while Model I is occasionally referenced to maintain consistency with broader biostratigraphic frameworks (e.g., Agnini et al., 2014; Fornaciari et al., 2010).

Event	Species	Base Zone*	Sample Base ID	Sample Top ID	Depth Base (mbsf)	Depth Top (mbsf)	Mid point (mbsf)	Chron position to the top	Age (Ma) GST 2012	Reference
T	*C. solitus*	NP17-CP14b	-	-	-	-	-	C18n.2n 0.21-C18n.1n 0.24	39.8 - 38.8	Agnini et al. 2014
Tc	*S. spiniger*	MNP17A	702B-8x-6w, 10	702B-8x-5w, 140	70.90	70.70	70.80	C18n.1n 0.94	40.10	Fornaciari et al. 2010
Bc	*D. bisectus*	CNE15	702B-9x-1w, 50	702B-9x-1w, 30	73.30	73.10	73.20	C18r 0.20	40.36	Agnini et al. 2014
Bc	*D. hesslandii*		702B-9x-2w, 20	702B-9x-1w, 140	74.50	74.20	74.35	C18r 0.22	40.37	Agnini et al. 2014
T	*S. furcatolithoides*	MNP16B	-	-	-	-	-	C18r 0.33	40.48	Agnini et al. 2014
Bc	*C. reticulatum*	CNE14	-	-	-	-	-	C19r 0.84	42.16	Agnini et al. 2014
Bc	*R. umbilicus*	NP16-CP14a-CNE13	-	-	-	-	-	C20n 0.42	42.77	Agnini et al. 2014

Table 5.1. Calcareous nannofossil biohorizons observed at Site ODP 702. The stratigraphic positions of each biohorizon are reported along with their corresponding sample depth (mbsf), the associated magnetic chron, and the calibrated ages (in Ma) according to both Edgar et al. (2010) and Westerhold & Röhl (2013). Biochronologic zonations follow Martini (1971), Okada & Bukry (1980), and Agnini et al. (2014). The interval analyzed spans the late Lutetian to early Bartonian and includes key events related to the Middle Eocene Climatic Optimum (MECO).

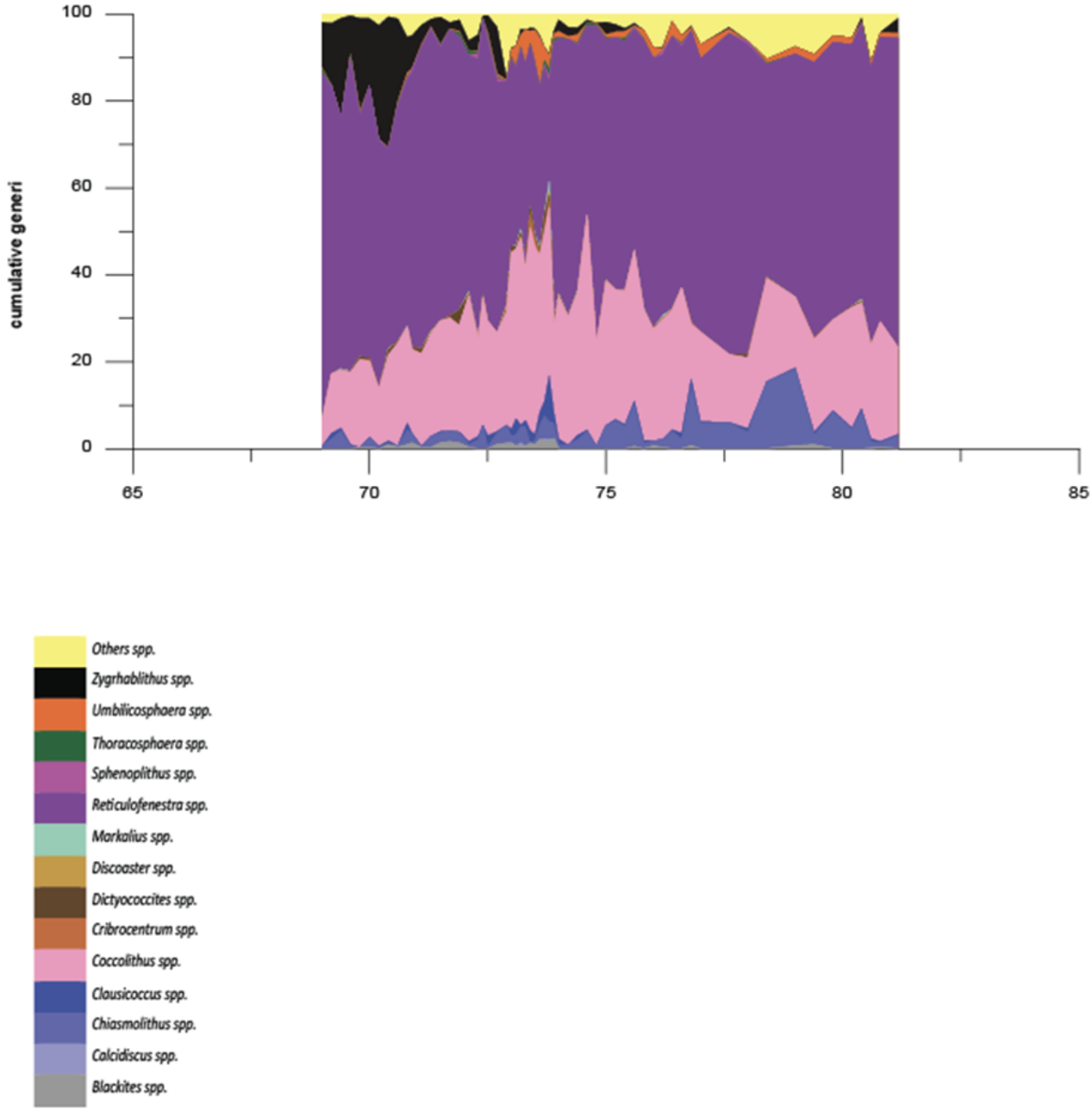

Figure 5.2. Cumulative relative abundance (%) of the main calcareous nannoplankton genera identified in the studied interval at ODP Site 7028. The y-axis represents depth in meters below seafloor (mbsf), and the x-axis shows the cumulative percentage of each genus. Taxa are color-coded as indicated in the legend. This graph illustrates major changes in assemblage composition across the studied interval

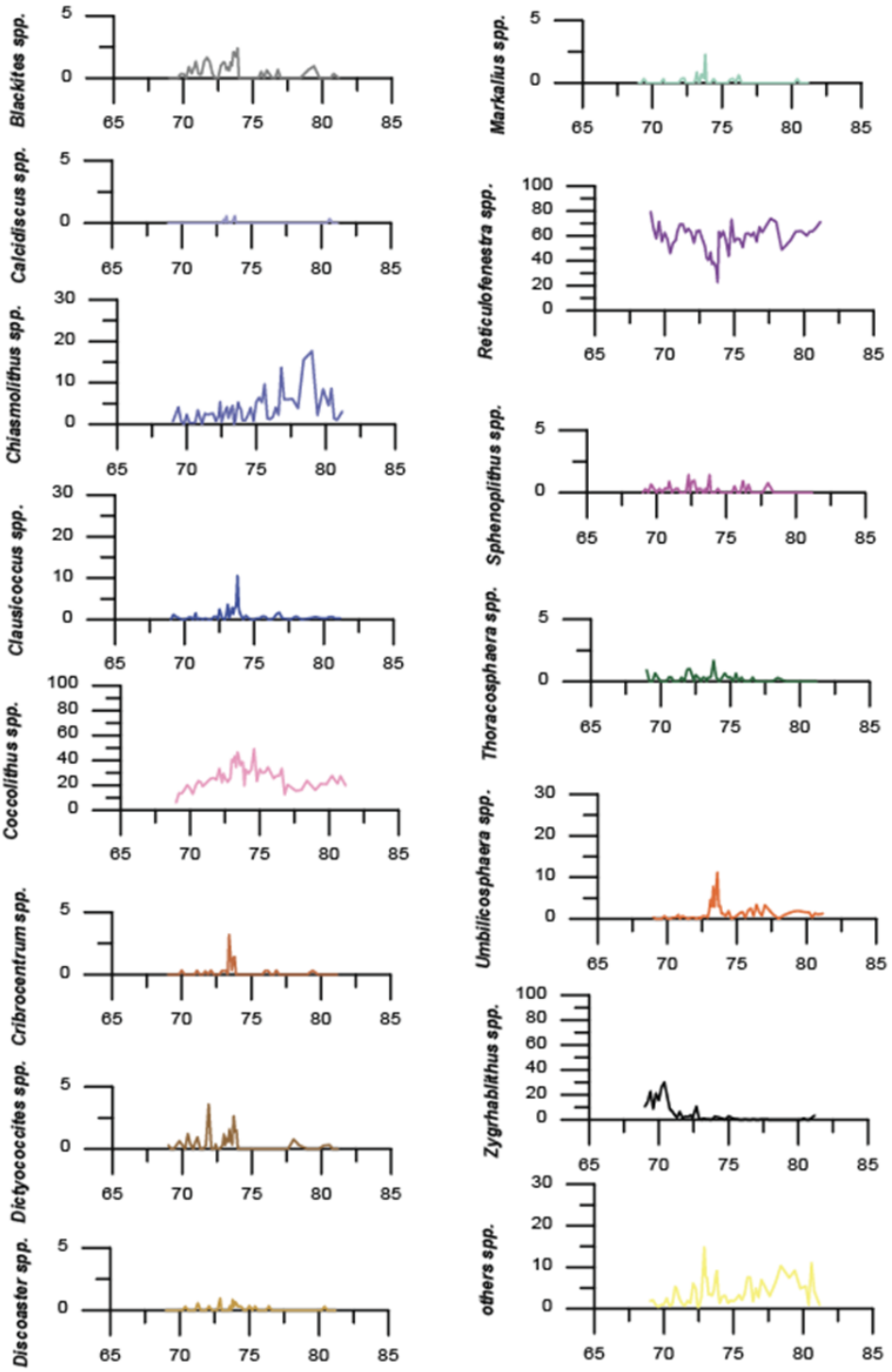

Figure 5.3. Relative abundances (%) of the main calcareous nannoplankton genera identified in the analyzed interval at ODP Site 702. The plotted data highlight stratigraphic variations in taxa distribution across the MECO interval.

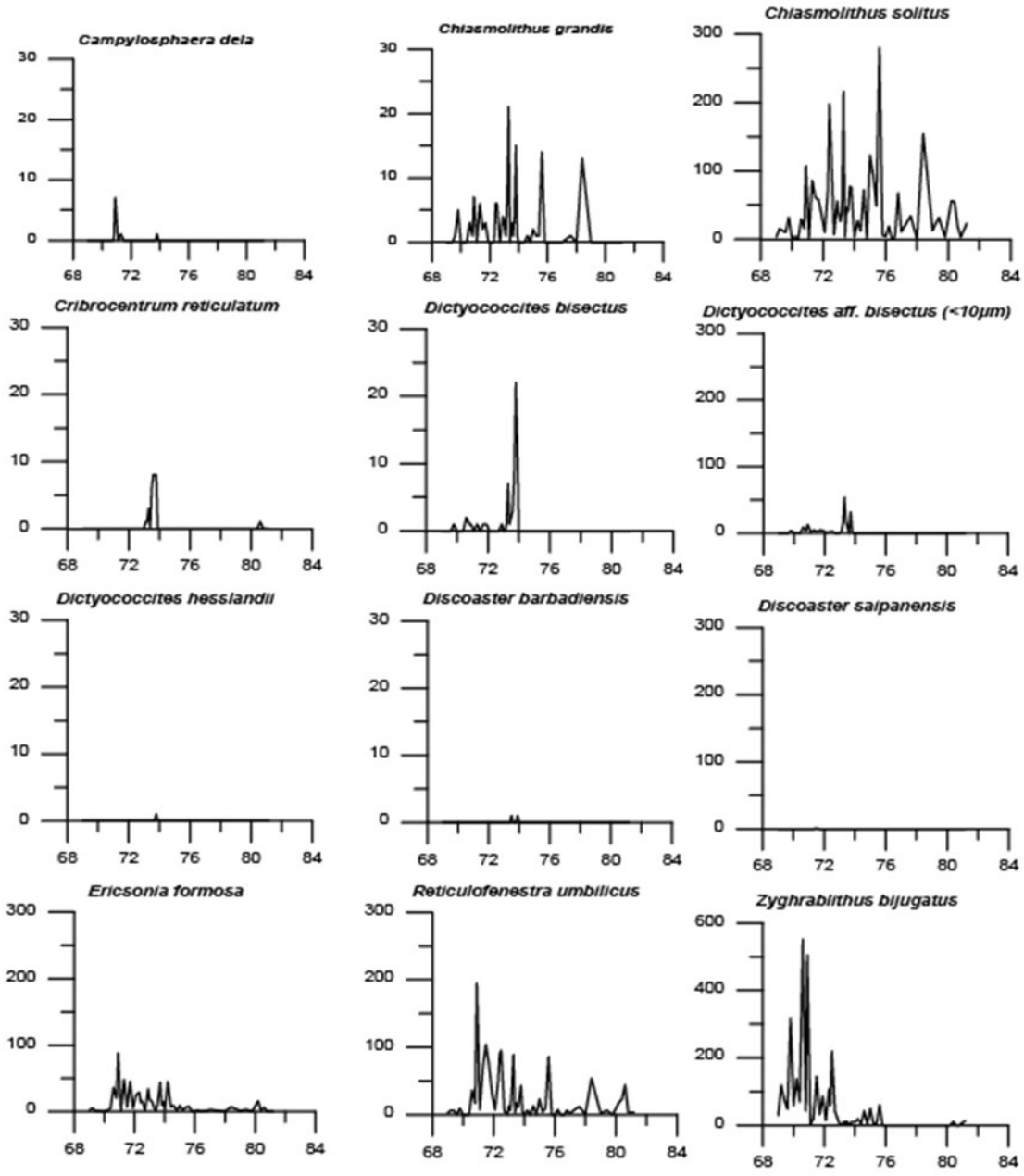

Figure 5.A.: Abundance (n/mm*) of selected calcareous nannofossil marker species plotted along the studied interval at ODP Site 702. The graphs represent the number of specimens of each taxon counted within a fixed area of smear slide, allowing for semi-quantitative biostratigraphic analysis.

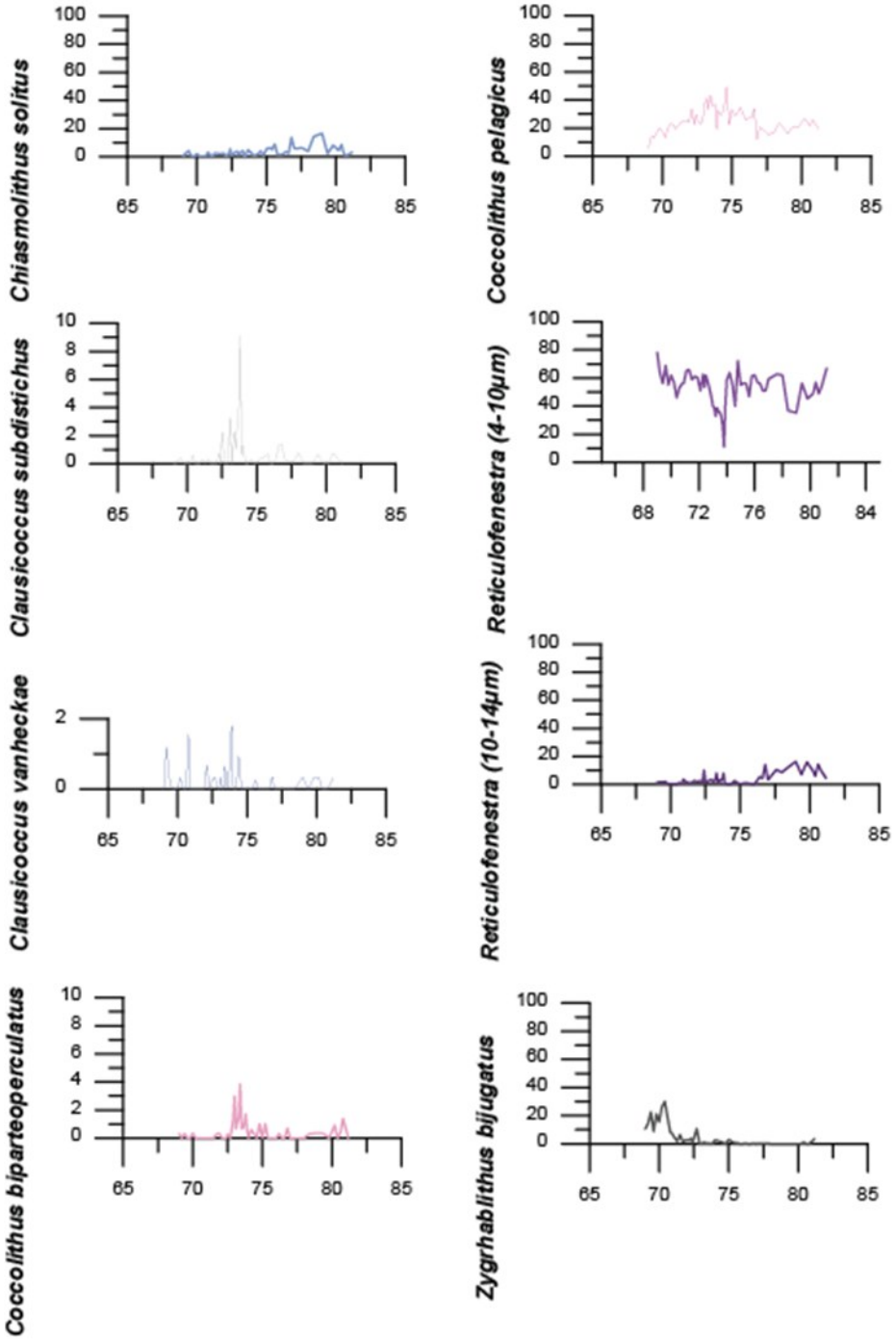

Figure 5.5.: Relative abundance (%) of selected calcareous nannofossil species that were relatively abundant throughout the studied interval at Hole ODP 7028.

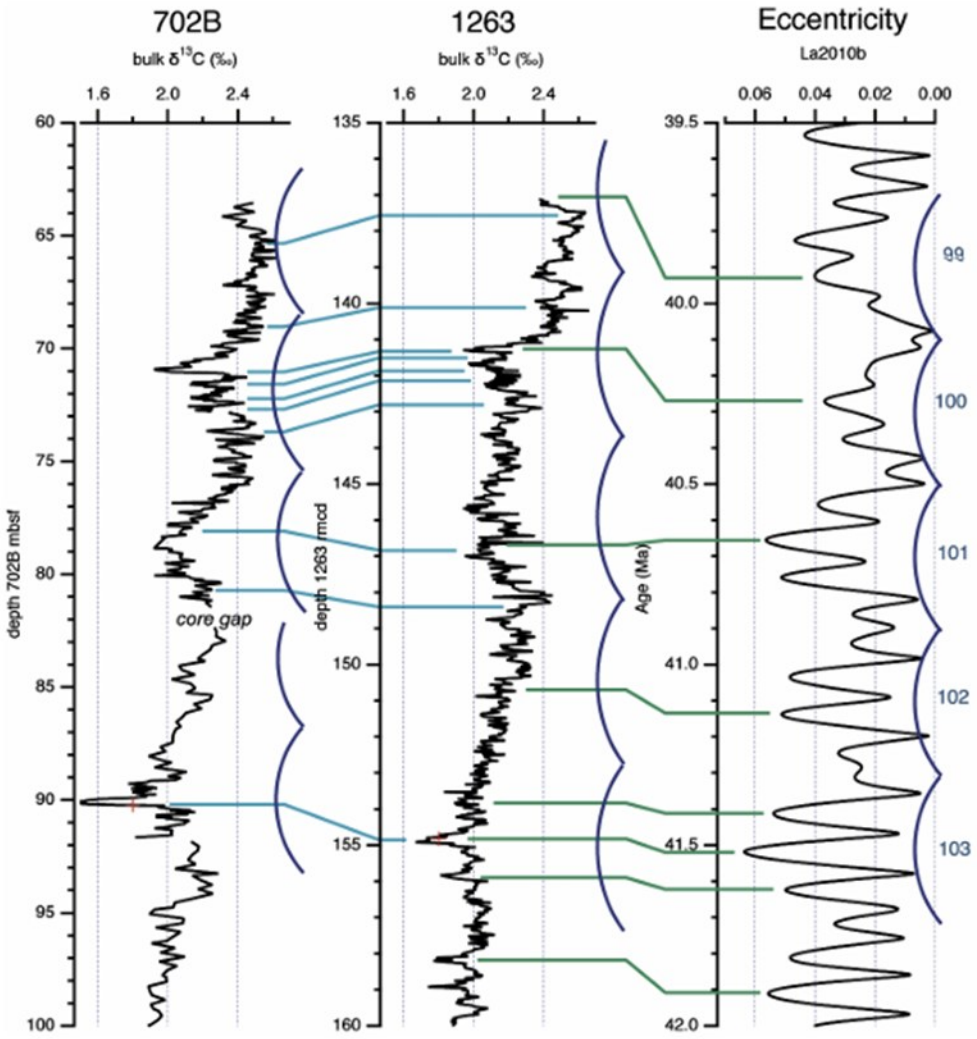

Figure 5.6. Age model for ODP Hole 702B derived by correlation to Site 1263 and calibrated using orbital tuning. Tie points between the two records are shown in blue, while green lines indicate eccentricity cycles used for age calibration. Modified from Rivero-Cuesta et al. (2019).

6. CONCLUSIONS

The analysis of calcareous nannofossil assemblages conducted in this study has provided a robust biostratigraphic and biochronologic framework for the sedimentary succession recovered at ODP Site 702B (Islas Orcadas Rise, South Atlantic). The integration of qualitative and quantitative micropaleontological data allowed for high-resolution calibration of the stratigraphy.

Biostratigraphic data allowed the studied interval to be confidently placed within standard calcareous nannofossil biozones. According to Martini (1971) and Okada & Bukry (1980), the studied section corresponds to Zone NP16 and Subzone CP14a. When applying the more recent schemes of Fornaciari et al. (2010) and Agnini et al. (2014), the succession falls within Subzones MNP16A–MNP16B and Zones CNE14/CNE15, respectively.

The age model applied to this site is based primarily on cyclostratigraphic tuning (Westerhold & Röhl, 2013), as adapted by Rivero-Cuesta et al. (2019) using $\delta^{13}C$ and $\delta^{18}O$ stable isotope records and XRF-based Fe content correlation to orbital solutions. The sampled interval (702B-9H-2W, 40 cm to 702B-8H-4W, 50 cm) spans from ~40.62 Ma to ~39.73 Ma, covering a duration of approximately 0.89 Myr and encompassing the late part of Chron C19n, the full extent of Chron C18r, and the base of Chron C18n.2n.

The biostratigraphic framework developed in this study confirms the order and timing of most bioevents recognized in previous literature (e.g., Fornaciari et al., 2010; Agnini et al., 2014). Compared to nearby Atlantic sites such as ODP 1263 and Site 702A, Site 702B shows excellent preservation and clear isotopic signals, allowing a reliable identification of biohorizons and climate trends.

Bibliography:

- Agnini, C., Fornaciari, E., Giusberti, L., Grandesso, P., Lanci, L., Luciani, V., Muttoni, G., Pälike, H., Rio, D., Spofforth, D. J. A., & Stefani, C. (2011). Integrated biomagnetostratigraphy of the Alano section (NE Italy): A proposal for defining the middle-late Eocene boundary. Bulletin of the Geological Society of America, 123(5), 841–872. https://doi.org/10.1130/B30158.1

- Agnini, C., Fornaciari, E., Raffi, I., Catanzariti, R., Pälike, H., Backman, J., & Rio, D. (2014). Biozonation and biochronology of Paleogene calcareous nannofossils from low and middle latitudes. Newsletters on Stratigraphy, 47(2), 131–181. https://doi.org/10.1127/0078-0421/2014/0042

- Archer, D., Kheshgi, H., & Maier-Reimer, E. (1997a). Multiple timescales for neutralization of fossil fuel CO2. Geophysical Research Letters, 24(4), 405–408. https://doi.org/10.1029/97GL00168

- Archer, D., Kheshgi, H., & Maier-Reimer, E. (1997b). Multiple timescales for neutralization of fossil fuel CO2. Geophysical Research Letters, 24(4), 405–408. https://doi.org/10.1029/97GL00168

- Backman, J. (n.d.). Quantitative Calcareous Nannofossil Biochronology of Middle Eocene through Early Oligocene Sediment from DSDP Sites 522 and 523. www.geologie.ac.at

- Backman, J., Raffi, I., Rio, D., Fornaciari, E., & Pälike, H. (2012). Biozonation and biochronology of miocene through pleistocene calcareous nannofossils from low and middle latitudes. Newsletters on Stratigraphy, 45(3), 221–244. https://doi.org/10.1127/0078-0421/2012/0022

- Berggren, W. A. . (1995). Geochronology, time scales and global stratification. SEPM.

- Bohaty, S. M., & Zachos, J. C. (2003). Significant Southern Ocean warming event in the late middle Eocene. In Geology. http://zeus.

- Bohaty, S. M., Zachos, J. C., Florindo, F., & Delaney, M. L. (2009a). Coupled greenhouse warming and deep-sea acidification in the middle Eocene. Paleoceanography, 24(2). https://doi.org/10.1029/2008PA001676

- Bohaty, S. M., Zachos, J. C., Florindo, F., & Delaney, M. L. (2009b). Coupled greenhouse warming and deep-sea acidification in the middle Eocene. Paleoceanography, 24(2). https://doi.org/10.1029/2008PA001676

- Cande, S. C., & Kent, D. v. (1995). Revised calibration of the geomagnetic polarity timescale for the late Cretaceous and Cenozoic. Journal of Geophysical Research, 100(B4), 6093–6095. https://doi.org/10.1029/94JB03098

- Coccolithophores. (2004). In Coccolithophores. Springer Berlin Heidelberg. https://doi.org/10.1007/978-3-662-06278-4

- Correction Pagani, M., Pedentchouk, N., Huber, M., Sluijs, A., Schouten, S., Brinkhuis, H., Damsté, J. S. S., Dickens, G. R., Backman, J., Clemens, S., Cronin, T., Eynaud, F., Gattacceca, J., Jakobsson, M., Jordan, R., Kaminski, M., King, J., Koc, N., Martinez, N. C., … Yamamoto, M. (2006). Arctic hydrology during global warming at the Palaeocene/Eocene thermal maximum. Nature, 442(7103), 671–675. https://doi.org/10.1038/nature05043

- Dickens, G. (n.d.). Methane oxidation during the Late Palaeocene Thermal Maximum. https://www.researchgate.net/publication/246812515

- Edgar, K. M., Wilson, P. A., Sexton, P. F., Gibbs, S. J., Roberts, A. P., & Norris, R. D. (2010). New biostratigraphic, magnetostratigraphic and isotopic insights into the Middle Eocene Climatic Optimum in low latitudes. Palaeogeography, Palaeoclimatology, Palaeoecology, 297(3–4), 670–682. https://doi.org/10.1016/j.palaeo.2010.09.016

- Edgar, K. M., Wilson, P. A., Sexton, P. F., & Suganuma, Y. (2007). No extreme bipolar glaciation during the main Eocene calcite compensation shift. Nature, 448(7156), 908–911. https://doi.org/10.1038/nature06053

- Fornaciari, E., Agnini, C., Catanzariti, R., Rio, D., Bolla, E. M., & Valvasoni, E. (2010). Mid-latitude calcareous nannofossil biostratigraphy and biochronology across the middle to late eocene transition. Stratigraphy, 7(4), 229–264. https://doi.org/10.29041/strat.07.4.01

- Henehan, M. J., Edgar, K. M., Foster, G. L., Penman, D. E., Hull, P. M., Greenop, R., Anagnostou, E., & Pearson, P. N. (2020). Revisiting the Middle Eocene Climatic Optimum "Carbon Cycle Conundrum" With New Estimates of Atmospheric pCO2 From Boron Isotopes. Paleoceanography and Paleoclimatology, 35(6). https://doi.org/10.1029/2019PA003713

- in developing principles, and providing a testing ground for various proposals contained in the Guide. (n.d.).

- Integrated Ocean Drilling Program Expedition 342 Preliminary Report Paleogene Newfoundland Sediment Drifts Expedition 342 Scientists. (n.d.). https://doi.org/10.2204/iodp.pr.342.2012

- Jovane, L., Florindo, F., Coccioni, R., Dinarès-Turell, J., Marsili, A., Monechi, S., Roberts, A. P., & Sprovieri, M. (2007a). The middle Eocene climatic optimum event in the Contessa Highway section, Umbrian Apennines, Italy. Bulletin of the Geological Society of America, 119(3–4), 413–427. https://doi.org/10.1130/B25917.1

- Jovane, L., Florindo, F., Coccioni, R., Dinarès-Turell, J., Marsili, A., Monechi, S., Roberts, A. P., & Sprovieri, M. (2007b). The middle Eocene climatic optimum event in the Contessa Highway section, Umbrian Apennines, Italy. Bulletin of the Geological Society of America, 119(3–4), 413–427. https://doi.org/10.1130/B25917.1

- Kennett, J. P., & Stott, L. D. (1991). Abrupt deep-sea warming, palaeoceanographic changes and benthic extinctions at the end of the Palaeocene. Nature, 353(6341), 225–229. https://doi.org/10.1038/353225a0

- Kerrick, D. M., & Caldeira, K. (1993). Paleoatmospheric consequences of CO 2 released during early Cenozoic regional metamorphism in the Tethyan orogen. In Chemical Geology (Vol. 108).

- Kerrick, D. M., & Caldeira, K. (1998). Metamorphic CO degassing from orogenic belts 2. In Chemical Geology (Vol. 145).

- Kerrick, D. M., & Caldeira, K. (1999). Was the Himalayan orogen a climatically significant coupled source and sink for atmospheric CO 2 during the Cenozoic? In Earth and Planetary Science Letters (Vol. 173). www.elsevier.com/locate/epsl

- Lourens, L. J., Sluijs, A., Kroon, D., Zachos, J. C., Thomas, E., Röhl, U., Bowles, J., & Raffi, I. (2005a). Astronomical pacing of late Palaeocene to early Eocene global warming events. Nature, 435(7045), 1083–1087. https://doi.org/10.1038/nature03814

- Lourens, L. J., Sluijs, A., Kroon, D., Zachos, J. C., Thomas, E., Röhl, U., Bowles, J., & Raffi, I. (2005b). Astronomical pacing of late Palaeocene to early Eocene global warming events. Nature, 435(7045), 1083–1087. https://doi.org/10.1038/nature03814

- Lyle, M., Olivarez Lyle, A., Backman, J., & Tripati, A. (n.d.-a). 21. BIOGENIC SEDIMENTATION IN THE EOCENE EQUATORIAL PACIFIC-THE STUTTERING GREENHOUSE AND EOCENE CARBONATE COMPENSATION DEPTH 1 (Vol. 199). http://www-odp.tamu.edu/

- Lyle, M., Olivarez Lyle, A., Backman, J., & Tripati, A. (n.d.-b). 21. BIOGENIC SEDIMENTATION IN THE EOCENE EQUATORIAL PACIFIC-THE STUTTERING GREENHOUSE AND EOCENE CARBONATE COMPENSATION DEPTH 1 (Vol. 199). http://www-odp.tamu.edu/

- Martini_1971_compressed (1). (n.d.).

- okada and Bukry1980. (n.d.).

- Pälike, H., Lyle, M. W., Nishi, H., Raffi, I., Ridgwell, A., Gamage, K., Klaus, A., Acton, G., Anderson, L., Backman, J., Baldauf, J., Beltran, C., Bohaty, S. M., Bown, P., Busch, W., Channell, J. E. T., Chun, C. O. J., Delaney, M., Dewangan, P., … Zeebe, R. E. (2012a). A Cenozoic record of the equatorial Pacific carbonate compensation depth. Nature, 488(7413), 609–614. https://doi.org/10.1038/nature11360

- Pälike, H., Lyle, M. W., Nishi, H., Raffi, I., Ridgwell, A., Gamage, K., Klaus, A., Acton, G., Anderson, L., Backman, J., Baldauf, J., Beltran, C., Bohaty, S. M., Bown, P., Busch, W., Channell, J. E. T., Chun, C. O. J., Delaney, M., Dewangan, P., … Zeebe, R. E. (2012b). A Cenozoic record of the equatorial Pacific carbonate compensation depth. Nature, 488(7413), 609–614. https://doi.org/10.1038/nature11360

- Pälike, H., Lyle, M. W., Nishi, H., Raffi, I., Ridgwell, A., Gamage, K., Klaus, A., Acton, G., Anderson, L., Backman, J., Baldauf, J., Beltran, C., Bohaty, S. M., Bown, P., Busch, W., Channell, J. E. T., Chun, C. O. J., Delaney, M., Dewangan, P., … Zeebe, R. E. (2012c). A Cenozoic record of the equatorial Pacific carbonate compensation depth. Nature, 488(7413), 609–614. https://doi.org/10.1038/nature11360

- Pälike, H., Norris, R. D., Herrle, J. O., Wilson, P. A., Coxall, H. K., Lear, C. H., Shackleton, N. J., Tripati, A. K., & Wade, B. S. (2006). The heartbeat of the Oligocene climate system. Science, 314(5807), 1894–1898. https://doi.org/10.1126/science.1133822

- Peterson, L. C., & Backman, J. (1990). Late Cenozoic Carbonate Accumulation and the History of the Carbonate Compensation Depth in the Western Equatorial Indian Ocean. In Proceedings of the Ocean Drilling Program, 115 Scientific Results. Ocean Drilling Program. https://doi.org/10.2973/odp.proc.sr.115.163.1990

- Rachmadhan, H. D., & Ruddiman, W. F. (n.d.). Past and Future.

- Rea, D. K., & Lyle, M. W. (2005a). Paleogene calcite compensation depth in the eastern subtropical Pacific: Answers and questions. Paleoceanography, 20(1), 1–19. https://doi.org/10.1029/2004PA001064

- Rea, D. K., & Lyle, M. W. (2005b). Paleogene calcite compensation depth in the eastern subtropical Pacific: Answers and questions. Paleoceanography, 20(1), 1–19. https://doi.org/10.1029/2004PA001064

- Rivero-Cuesta, L., Westerhold, T., Agnini, C., Dallanave, E., Wilkens, R. H., & Alegret, L. (2019). Paleoenvironmental Changes at ODP Site 702 (South Atlantic): Anatomy of the Middle Eocene

Climatic Optimum. Paleoceanography and Paleoclimatology, 34(12), 2047–2066. https://doi.org/10.1029/2019PA003806

- ROL_4_5. (n.d.).

- Salvador, Amos. (2013). International stratigraphic guide : a guide to stratigraphic classification, terminology, and procedure. International Union of Geological Sciences ; Geological Society of America.

- SCIENZE MM FF NN Dipartimento di Geoscienze Direttore Profssa Cristina Stefani, F. di, Claudia Agnini Laureando, P., & Menini, A. (n.d.). UNIVERSITÀ DEGLI STUDI DI PADOVA STUDIO BIOSTRATIGRAFICO E RISPOSTA PALEOECOLOGICA DELLE ASSOCIAZIONI A NANNOFOSSILI CALCAREI DURANTE IL MIDDLE EOCENE CLIMATIC OPTIMUM (MECO) AL SITE ODP 929, (CEARA RISE, ATLANTICO EQUATORIALE).

- Sexton, P. F., Wilson, P. A., & Norris, R. D. (2006a). Testing the Cenozoic multisite composite δ18O and δ13C curves: New monospecific Eocene records from a single locality, Demerara Rise (Ocean Drilling Program Leg 207). Paleoceanography, 21(2). https://doi.org/10.1029/2005PA001253

- Sexton, P. F., Wilson, P. A., & Norris, R. D. (2006b). Testing the Cenozoic multisite composite δ18O and δ13C curves: New monospecific Eocene records from a single locality, Demerara Rise (Ocean Drilling Program Leg 207). Paleoceanography, 21(2). https://doi.org/10.1029/2005PA001253

- Spofforth, D. J. A., Agnini, C., Pälike, H., Rio, D., Fornaciari, E., Giusberti, L., Luciani, V., Lanci, L., & Muttoni, G. (2010). Organic carbon burial following the middle Eocene climatic optimum in the central western Tethys. Paleoceanography, 25(3). https://doi.org/10.1029/2009PA001738

- Suganuma, Y., & Ogg, J. G. (2005). Campanian through Eocene magnetostratigraphy of Sites 1257-1261, ODP leg 207, Demerara Rise (western equatorial Atlantic). Proceedings of the Ocean Drilling Program: Scientific Results, 207. https://doi.org/10.2973/odp.proc.sr.207.102.2006

- Toffanin et al_2013_ Micropaleontology. (n.d.).

- Toffanin, F., Agnini, C., Fornaciari, E., Rio, D., Giusberti, L., Luciani, V., Spofforth, D. J. A., & Pälike, H. (2011). Changes in calcareous nannofossil assemblages during the Middle Eocene Climatic Optimum: Clues from the central-western Tethys (Alano section, NE Italy). Marine Micropaleontology, 81(1–2), 22–31. https://doi.org/10.1016/j.marmicro.2011.07.002

- Tripati, A., Backman, J., Elderfield, H., & Ferretti, P. (2005). Eocene bipolar glaciation associated with global carbon cycle changes. Nature, 436(7049), 341–346. https://doi.org/10.1038/nature03874

- Vahlenkamp, M., Niezgodzki, I., de Vleeschouwer, D., Bickert, T., Harper, D., Kirtland Turner, S., Lohmann, G., Sexton, P., Zachos, J., & Pälike, H. (2018). Astronomically paced changes in deep-water circulation in the western North Atlantic during the middle Eocene. Earth and Planetary Science Letters, 484, 329–340. https://doi.org/10.1016/j.epsl.2017.12.016

- van der Ploeg, R., Selby, D., Cramwinckel, M. J., Li, Y., Bohaty, S. M., Middelburg, J. J., & Sluijs, A. (2018). Middle Eocene greenhouse warming facilitated by diminished weathering feedback. Nature Communications, 9(1). https://doi.org/10.1038/s41467-018-05104-9

- Viganò, A., Westerhold, T., Bown, P. R., Jones, T. D., & Agnini, C. (2023). Calcareous nannofossils across the Eocene-Oligocene transition: Preservation signals and biostratigraphic remarks from ODP Site 1209 (NW Pacific, Shatsky Rise) and IODP Hole U1411B (NW Atlantic Ocean, Newfoundland Ridge). Palaeogeography, Palaeoclimatology, Palaeoecology, 629. https://doi.org/10.1016/j.palaeo.2023.111778

- Villa, G., Fioroni, C., Pea, L., Bohaty, S., & Persico, D. (2008). Middle Eocene-late Oligocene climate variability: Calcareous nannofossil response at Kerguelen Plateau, Site 748. Marine Micropaleontology, 69(2), 173–192. https://doi.org/10.1016/j.marmicro.2008.07.006

- Wade, B. S., Pearson, P. N., Berggren, W. A., & Pälike, H. (2011). Review and revision of Cenozoic tropical planktonic foraminiferal biostratigraphy and calibration to the geomagnetic polarity and astronomical time scale. In Earth-Science Reviews (Vol. 104, Issues 1–3, pp. 111–142). https://doi.org/10.1016/j.earscirev.2010.09.003

- Wei, W., & Wise, S. W. (1990). Biogeographic gradients of middle Eocene-Oligocene calcareous nannoplankton in the South Atlantic Ocean. In Palaeogeography, Palaeoclimatology, Palaeoecology.

- Westerhold, T., & Röhl, U. (2013a). Orbital pacing of Eocene climate during the Middle Eocene Climate Optimum and the chron C19r event: Missing link found in the tropical western Atlantic. Geochemistry, Geophysics, Geosystems, 14(11), 4811–4825. https://doi.org/10.1002/ggge.20293

- Westerhold, T., & Röhl, U. (2013b). Orbital pacing of Eocene climate during the Middle Eocene Climate Optimum and the chron C19r event: Missing link found in the tropical western Atlantic. Geochemistry, Geophysics, Geosystems, 14(11), 4811–4825. https://doi.org/10.1002/ggge.20293

- Zachos, J. C., Dickens, G. R., & Zeebe, R. E. (2008a). An early Cenozoic perspective on greenhouse warming and carbon-cycle dynamics. In Nature (Vol. 451, Issue 7176, pp. 279–283). Nature Publishing Group. https://doi.org/10.1038/nature06588

- Zachos, J. C., Dickens, G. R., & Zeebe, R. E. (2008b). An early Cenozoic perspective on greenhouse warming and carbon-cycle dynamics. In Nature (Vol. 451, Issue 7176, pp. 279–283). Nature Publishing Group. https://doi.org/10.1038/nature06588

- Zachos, J. C., Kroon, D., Blum, P., & Bowles, J. A. (2004a). Early Cenozoic extreme Climates: The Walvis Ridge transect. https://www.researchgate.net/publication/282323186

- Zachos, J. C., Kroon, D., Blum, P., & Bowles, J. A. (2004b). Early Cenozoic extreme Climates: The Walvis Ridge transect. https://www.researchgate.net/publication/282323186

- Zachos, J. C., McCarren, H., Murphy, B., Röhl, U., & Westerhold, T. (2010). Tempo and scale of late Paleocene and early Eocene carbon isotope cycles: Implications for the origin of hyperthermals. Earth and Planetary Science Letters, 299(1–2), 242–249. https://doi.org/10.1016/j.epsl.2010.09.004

- Zachos, J., Pagani, H., Sloan, L., Thomas, E., & Billups, K. (2001a). Trends, rhythms, and aberrations in global climate 65 Ma to present. In Science (Vol. 292, Issue 5517, pp. 686–693). https://doi.org/10.1126/science.1059412

- Zachos, J., Pagani, H., Sloan, L., Thomas, E., & Billups, K. (2001b). Trends, rhythms, and aberrations in global climate 65 Ma to present. In Science (Vol. 292, Issue 5517, pp. 686–693). https://doi.org/10.1126/science.1059412